

Lawrence Berkeley National Laboratory

Lawrence Berkeley National Laboratory

Title

Laser ablation of electronic materials including the effects of energy coupling and plasma interactions

Permalink

<https://escholarship.org/uc/item/1c56k8x2>

Author

Zeng, Xianzhong

Publication Date

2004-12-10

**Laser Ablation of Electronic Materials Including the Effects of
Energy Coupling and Plasma Interactions**

by

Xianzhong Zeng

B.Eng. (Tsinghua University, China) 1997

M.Eng. (Tsinghua University, China) 2000

**A dissertation submitted in partial satisfaction of the
requirements for the degree of**

Doctor of Philosophy

in

Engineering - Mechanical Engineering

in the

GRADUATE DIVISION

of the

UNIVERSITY OF CALIFORNIA, BERKELEY

Committee in charge:

Professor Ralph Greif, Chair

Professor Costas P. Grigoropoulos

Professor Vivek Subramanian

Fall 2004

Abstract

Laser Ablation of Electronic Materials Including the Effects of Energy Coupling and Plasma Interactions

Xianzhong Zeng

Doctor of Philosophy in Engineering

University of California at Berkeley

Professor Ralph Greif, Chair

Many laser ablation applications such as laser drilling and micromachining generate cavity structures. The study of laser ablation inside a cavity is of both fundamental and practical significance. In this dissertation, cavities with different aspect ratios (depth/diameter) were fabricated in fused silica by laser micromachining. Pulsed laser ablation in the cavities was studied and compared with laser ablation on a flat surface. The formation of laser-induced plasmas in the cavities and the effects of the cavities on the ablation processes were investigated. The temperatures and electron number densities of the resulting laser-induced plasmas in the cavities were determined from spectroscopic measurements. Reflection and confinement effects by the cavity walls and plasma shielding were discussed to explain the increased temperature and electron number density with respect to increasing cavity aspect ratio. The temporal variations of the plasma temperature and electron number density inside the cavity decreased more rapidly

than outside the cavity. The effect of laser energy on formation of a plasma inside a cavity was also investigated.

Propagation of the shock wave generated during pulsed laser ablation in cavities was measured using laser shadowgraph imaging and compared with laser ablation on a flat surface. It is found that outside the cavity, after about 30 ns the radius of the expanding shock wave was proportional to $t^{2/5}$, which corresponds to a spherical blast wave. The calculated pressures and temperatures of the shocked air outside of the cavities were higher than those obtained on the flat surface.

Lasers with femtosecond pulse duration are receiving much attention for direct fabrication of microstructures due to their capabilities of high-precision ablation with minimal damage to the sample. We have also performed experimental studies of pulsed femtosecond laser ablation on the flat surface of silicon samples and compared results with pulsed nanosecond laser ablation at a ultraviolet wavelength (266 nm). Crater depth measurements indicated that ablation efficiency was enhanced for UV femtosecond laser pulses. The electron number densities and temperatures of femtosecond-pulse plasmas decreased faster than nanosecond-pulse plasmas due to different energy deposition mechanisms. Plasma expansion in both the perpendicular and the lateral directions were studied.

Professor Ralph Greif, Committee Chair

Table of Contents

Chapter 1	Introduction	
1.1	Laser-Material Interactions: Overview	1
1.2	Scope of Research	6
	References	8
Chapter 2	Influence of Cavity Dimensions on Laser Ablation in Cavity Structures	
2.1	Introduction	11
2.2	Experimental system	12
2.3	Results and discussion	15
	2.3.1 Spectral line analysis	15
	2.3.2 Electron number density and plasma temperature	19
	2.3.3 Effect of cavity aspect ratio	22
	2.3.4 Temporal evolution of plasma properties	26
2.4	Conclusions	33
	References	34
Chapter 3	Dependence of Properties of Laser-Induced Plasma in a Cavity on Laser Irradiance	
3.1	Introduction	36

3.2	Experimental system	37
3.3	Results and discussion	38
3.3.1	Electron number density and plasma temperature calculation: second ionization effects	39
3.3.2	Effect of laser energy on formation of a plasma inside a cavity	43
3.4	Conclusions	55
	References	57
Chapter 4	Energy Deposition and Shock Wave Propagation during Pulsed Laser Ablation in Cavities	
4.1	Introduction	59
4.2	Experimental System	60
4.3	Results and discussion	61
4.3.1	Shadowgraph images of the shock waves generated from laser ablation in cavities	61
4.3.2	A modified blast wave equation for shock wave generated from laser ablation in cavities	67
4.3.3	Thermodynamic properties of the shocked air	69
4.4	Conclusions	71
	References	72

Chapter 5	Ablation Efficiency and Plasma Expansion during Ultraviolet Femtosecond and Nanosecond Laser Ablation of Silicon	
5.1	Introduction	73
5.2	Experimental system	74
5.3	Results and discussion	76
	5.3.1 Ablation depth	76
	5.3.2 Plasma temperature and electron number density comparison	81
	5.3.3 Plasma expansion	86
5.4	Conclusions	87
Chapter 6	Conclusions and Future Research	
6.1	Conclusions	94
6.2	Future Research	96

List of Figures

- Figure 1.1 Complex microstructures fabricated by laser-assisted microstereolithography process
- Figure 1.2 SEM photograph of a hole drilled in a steel foil with 200 fs, 120 μ J laser pulses at 780 nm.
- Figure 1.3 Laser ablation of fused silica at time of 110 ns.
- Figure 2.1 Experimental system for spectroscopic measurements of laser-induced plasma.
- Figure 2.2 Cavities formed during repetitive laser ablation in fused silica. (a) 80-micron diameter, 480-micron depth cavity formed after 700 pulses laser ablation at an irradiance of 2.9 GW/cm^2 . (b) 165-micron diameter, 485-micron depth cavity formed after 850 pulses laser ablation at an irradiance of 2.1 GW/cm^2 . (c) 490-micron diameter, 480-micron depth cavity formed after 1100 pulses laser ablation at an irradiance of 1.5 GW/cm^2 . The bold lines are schematic cross-sections of the cavities.
- Figure 2.3 (a) Spatial distributions of plasma emission from the 160-micron diameter cavity (depth 480 micron) in silica at wavelength of Si(I) 288.16 nm and time of 100 ns. Irradiance was 15.9 GW/cm^2 . (b) Spatial distributions of plasma emission from the flat surface at

wavelength of 288.16 nm and time of 100 ns, irradiance was 15.6 GW/cm².

- Figure 2.4 Lorentzian fitting of the Stark broadened profile for Si 288.16 nm. The full width half maximum (FWHM) was used for the calculation of the electron number density. The ratio of the integrated spectral line intensity (A) and continuum intensity (y_0) at the center wavelength (x_c) were used for the calculation of plasma temperature.
- Figure 2.5 (a) Plasma temperature and (b) electron number density vs. distance from surface. Compare effect of diameter at time of 100 ns and an irradiance of 6.95 GW/cm².
- Figure 2.6 (a) Temporal evolution of plasma temperature and (b) Electron number density vs. distance from surface. Compare cavity (Diameter 85 micron, depth 500 micron) and flat surface ablation results, irradiance is 7.95 GW/cm².
- Figure 2.7 (a) Temporal evolution of plasma temperature inside and outside of the cavity. (b) Temporal evolution of electron number densities inside and outside of the cavity. Cavity diameter is 80 micron and depth 480 micron. Irradiance is 7.67 GW/cm².
- Figure 3.1 Si(I) 288.16 nm spectral line and continuum emission at time of 30 ns, distance of 1 mm and irradiance of 15 GW/cm². Compare flat surface and cavity (Diameter 250 micron, depth 500 micron) ablation results. Bold lines are Lorentzian fitting curves.

- Figure 3.2 (a) Electron number density and (b) plasma temperature vs. irradiance. Compare flat surface and two cavity (Diameter 130 micron, depth 500 micron, aspect ratio 4; Diameter 250 micron, depth 500 micron, aspect ratio 2) ablation results at time of 30 ns and distance of 1mm. Sample was fused silica.
- Figure 3.3 Electron number density and plasma temperature vs. distance from surface at below and above threshold irradiances. Compare (a, b) flat surface and (c, d) cavity (Diameter 130 micron, depth 500 micron) ablation results at time of 30 ns.
- Figure 3.4 Silicon ionization efficiency vs. irradiance. Compare (a) flat surface and two cavity ((b) Diameter 130 micron, depth 500 micron, aspect ratio 4; (c) Diameter 250 micron, depth 500 micron, aspect ratio 2) ablation results at time of 30 ns and distance of 1 mm.
- Figure 3.5 Inverse bremsstrahlung absorption coefficient at time of 30 ns and distance of 1 mm vs. irradiance.
- Figure 3.6 Crater depth resulting from single pulse laser ablation on fused silica vs. irradiance.
- Figure 3.7 Images obtained by laser shadowgraphy for laser irradiances of (a) 21 GW/cm^2 and (b) 18 GW/cm^2 at time of $2 \mu\text{s}$.
- Figure 4.1 Schematic of the experimental setup for the pump-probe technique.
- Figure 4.2 Shadow-graphic images of shock wave generated from laser ablation in cavity (a) and on flat surface (b). Cavity depth $240 \mu\text{m}$,

diameter 80 μm . The shock front (S), the ionization front (I), contact front (C) and back pressure induced shock wave (B) are labeled in the figures.

Figure 4.3 Shadow-graphic images of shock wave generated from laser ablation in cavity at laser energy 0.5 mJ (a) and 1.9 mJ (b). Cavity depth 480 μm , diameter 80 μm . The detonation wave (D) and ejected materials (M) are labeled in the figures.

Figure 4.4 Air shock wave radius as a function of time for laser ablation in cavities and on flat surface.

Figure 5.1 Ablation depth vs. pulse number for femtosecond and nanosecond laser ablation. The insets show the fs and ns crater profile after five laser pulses.

Figure 5.2 SEM images of laser generated silicon particles (A, C from nanosecond laser ablation with 5000 and 20000 magnification rates; B, D from femtosecond laser ablation with 5000 and 20000 magnification rates. Particles were collected on a silicon substrate).

Figure 5.3 Peak intensity of Si (I) 288.16 nm emission line as a function of time for femtosecond and nanosecond laser ablation at a distance of 0.6 mm above the target surface.

Figure 5.4 Plasma temperature (A) and electron number density (B) as a function of time for femtosecond and nanosecond laser ablation at a distance of 0.6 mm above the target surface.

- Figure 5.5 Plasma images obtained by laser shadowgraphy for femtosecond (a) and nanosecond (b) laser ablation at 10 ns after laser shot. The shock front (S), ionization front (I), contact front (C) and air breakdown plasma (A) are labeled in the figures.
- Figure 5.6 Sequence of shock wave images obtained by laser shadowgraphy for femtosecond (a-d) and nanosecond (e-h) laser ablation.
- Figure 5.7 Perpendicular (A) and lateral (B) expansion distance of shock wave as a function of time for femtosecond and nanosecond laser ablation.

List of Tables

- Table 2.1 The parameters used for plasma temperature and electron number density calculations.
- Table 3.1 Coefficients for partition functions of silicon atom, singly-charged and doubly-charged silicon ions.
- Table 4.1 Thermodynamic properties of the shocked air just behind the shock wave front at time of 20 ns after the shock wave expands outside of the cavity.

Chapter 1

INTRODUCTION

1.1 Laser-Material Interactions: Overview

Experimental investigations of laser interactions with solid materials began soon after the introduction of the first ruby laser in 1960. Since the 1970s, solid state Nd:YAG lasers are commonly used for laser-material interactions research because they are more stable and deliver optically superior beams. With the development of the chirped pulse amplification technique [1] in the 1980s, ultrashort laser pulse durations in picoseconds and even femtoseconds can be achieved. The versatility of solid state lasers, especially with variable pulse durations and tunable wavelength, contributes to the tremendous progress in laser-material interactions research and applications.

With the advanced lasers, laser processing of semiconductors, microstructures and thin films began to attract enormous interest since the late 1970s. For example, a recently developed laser-assisted micro-stereolithography technique [2] can produce highly precise, three-dimensional microstructures (Figure 1), providing an engineering platform for various applications, such as Microelectromechanical Systems (MEMS). Laser-assisted techniques in these areas include laser annealing [3], laser cleaning of surfaces [4], lithography [5], etching [6] and drilling [7].

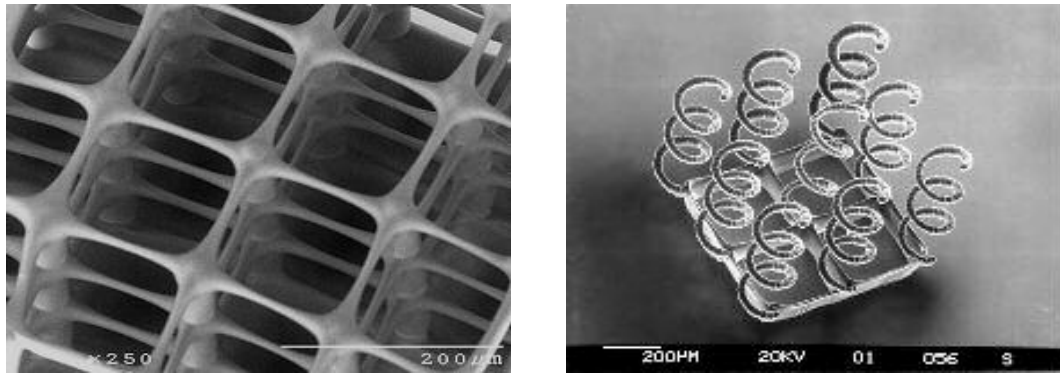


Figure 1.1 Complex microstructures fabricated by laser-assisted microstereolithography process.

In order to continue semiconductor device scaling and improve device performance, shallow and abrupt junctions with low sheet resistance are required for the source and drain extensions to reduce the parasitic resistance [8]. For conventional thermal annealing, low sheet resistance is limited by solid solubility and abruptness is limited by implantation and diffusion mechanisms. Laser annealing can be an attractive candidate for making box-shaped highly-doped ultrashallow source and drain extension junctions [9,10,11]. Device performance can be further improved for smaller gate length and thinner gate oxide devices with laser annealing because Source/Drain is a substantial fraction of the overall device resistance in this case.

Mass removal and plasma formation often occur when a target material is irradiated by a high-power laser beam. Laser ablation [12] refers to this explosive laser-material-interaction. The mass removed and laser-induced plasma are dependent on the laser beam parameters (pulse duration, energy, and wavelength),

the solid target properties and the surrounding environment. Laser ablation is a powerful technology for direct material analysis [13], thin film deposition [14], micromachining [15] and medical applications [16].

Laser ablation is an excellent technology for directly vaporizing solid samples for elemental analysis with inductively-coupled plasma atomic emission spectroscopy and mass spectrometry. In laser-induced breakdown spectroscopy (LIBS), a laser is used to ablate and atomize material from a sample and to create a plasma whose emission is used to identify and quantify elements within the sample. The ability to nondestructively analyze unprepared samples makes LIBS a highly versatile analytical technique. Its range of applications is growing rapidly, including environmental [17, 18], art [19] and medical [20] analyses.

Pulsed-laser deposition (PLD) uses laser pulses to ablate material from a target and deposit it onto a substrate. Pulsed laser deposition of thin films offers several advantages over conventional methods such as chemical vapor deposition or physical vapor deposition. It is a clean and fast process. The film thickness can be precisely controlled. Stoichiometry of deposited films can be controlled by selecting shorter wavelengths and shorter pulses [21].

Compared with traditional wet or dry etching, laser micromachining has the advantage of direct-write capability which saves the expensive lithography steps. Laser micromachining can also enable three-dimensional fabrication of microstructures. Presently, lasers with femtosecond pulse duration are gaining more attention for micromachining as the pulse duration is less than the typical

thermalization characteristic time of a few picoseconds. Due to a much smaller thermal diffusion depth, high-precision ablation and minimal damage can be obtained with femtosecond lasers [22, 23]. Figure 2 shows a Scanning Electron Microscope (SEM) photograph of a hole drilled by a femtosecond laser in a steel foil. Because of its short pulse duration, the femtosecond laser beam does not interact with the laser-induced plasma. Absorbed laser energy is fully deposited on the target and higher efficiency of material ablation can be obtained [24].

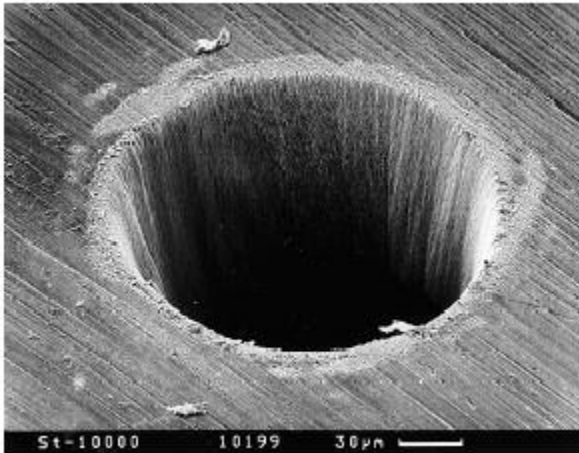


Figure 1.2 SEM photograph of a hole drilled in a steel foil with 200 fs, 120 μ J laser pulses at 780 nm.

Efficient use of lasers for material processing requires the fundamental knowledge of the interactions of the laser radiation with matter. Coupling intense electromagnetic energy of a laser pulse with a target material can result in melting, vaporization, ejection of atoms, ions, and molecular species, as well as shock wave

formation and plasma development [25]. Figure 3 is a laser shadowgraph image of laser ablation of fused silica which shows ejection of target materials as well as a laser-induced plasma.

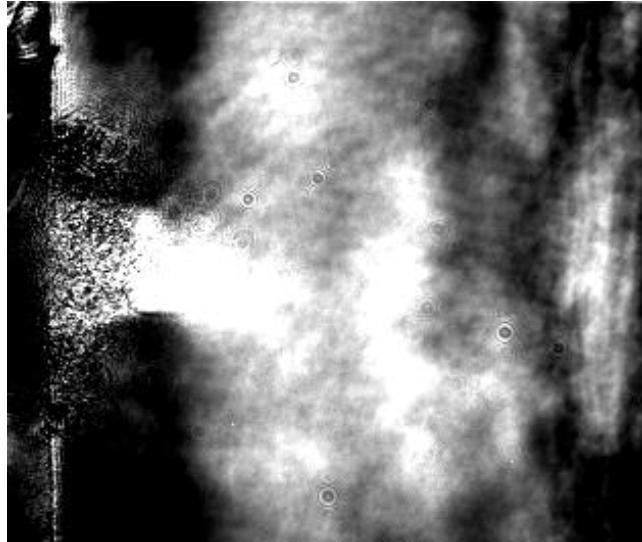


Figure 1.3 Laser ablation of fused silica at time of 110 ns and irradiance of 210 GW/cm^2 . The nanosecond laser beam was focused on the sample to a spot diameter of ~ 50 microns in air.

In high-power laser ablation, a laser-induced plasma can influence the ablation process greatly. The expanding plasma can interact with the later portion of the laser pulse and thereby reduce the laser energy reaching the target surface. Mao [26] reported that a high electron density plasma formed during picosecond laser ablation is responsible for the reduction of mass removal at high laser fluences. The dynamics of plume expansion is also important for the pulsed laser deposition process and nanoparticles generation.

The primary research in this dissertation is the ablation process in cavity structures. In many laser–material interaction applications such as micro-machining and solid sampling for chemical analysis, cavity structures with specific aspect ratios (depth-to-diameter ratio) develop after repetitive pulses irradiate the same target location. As a consequence, the laser interaction is with the resulting cavity structure, rather than the flat surface. Although most theoretical investigations have been devoted to laser ablation on a flat surface, the fundamental processes of laser interactions with a cavity structure remains largely unexplored.

1.2 Scope of Research

The scope of this research was to investigate laser ablation inside cavity structures, in particular, to study the laser-induced plasmas that developed inside and outside cavities of different aspect ratios. The effects of cavity aspect ratio and laser energy on plasma properties were investigated. The temperature and electron number density of laser-induced plasmas were measured and found to be much higher and to decrease faster for a plasma inside a cavity than that from a flat surface. Cavity wall influences on the plasma expansion are discussed.

Femtosecond lasers have the advantage of minimizing thermal effects which is important for applications such as laser micro-fabrication. In addition to the studies of laser plasmas in cavities, this research also includes comparisons of ultrafast laser plasmas between femtosecond and nanosecond laser ablation on a flat surface.

The dissertation is organized as follows. In chapter 2, the effects of cavity aspect ratio on laser-induced plasma properties are investigated. The temperature and electron number density of laser-induced plasmas in fused silica cavities are determined using spectroscopic methods. Chapter 3 presents experimental investigation of the effect of laser energy on formation of the laser plasma inside the cavity. In chapter 4, measurements of the propagation of the shock wave generated during pulsed laser ablation in cavities are reported using laser shadowgraph imaging and compared with laser ablation on a flat surface.

Chapter 5 presents experimental investigation of ablation efficiency and plasma expansion during femtosecond and nanosecond laser ablation of silicon at ultraviolet wavelength (266 nm). Laser ablation efficiency is studied by measuring crater depth as a function of pulse number. The temperature and electron number density of the pulsed laser-induced plasma are determined from spectroscopic measurements. Plasma expansion is studied with laser shadowgraph imaging technique.

Chapter 6 includes the conclusions of the present study and a recommendation for future research directions.

REFERENCE

1. D. Strickland, G. Mourou, Compression of amplified chirped optical pulses, *Opt. Commun.* **56**, 219 (1985)
2. X. Zhang, X.N. Jiang and C. Sun, *Sensors and Actuators A (Physical)*, **A77**, 149 (1999)
3. Hironori Tsukamoto and Toshiharu Suzuki, *Solid-State Electronics*, **42**, 547 (1998)
4. W. Zapka, W. Ziemlich, W.P. Leung and A.C. Tam, *Microel. Engin.*, **20**, 171 (1993)
5. K. Jain, *Excimer laser lithography* (SPIE Optical Engineering Press, Bellingham, WA, 1990)
6. G. T. A. Kovacs, N. I. Maluf and K. E. Petersen, *Proc. IEEE*, **86**, 1536 (1998)
7. J. F., Ready, *Industrial Applications of Lasers* (Academic Press, New York, 1978)
8. The National Technology Roadmap for Semiconductors, Semiconductor Industry Association, San Jose, CA, 1994
9. Eun Sik Jung, Ji chel Bea and Yong Jae Lee, *IEEE, ISIE*, Pusan, Korea, 586 (2001)
10. Susan Earles, Mark Law, Richard Brindos, Kevin Jones, Somit Talwar and Sean Corcoran, *IEEE Transactions on Electron Devices*, **49**, 1118 (2002)
11. Seong-Dong Kim, Cheol-Min Park and Jason C.S. Woo, *IEEE Transactions on Electron Devices*, **49**, 1748 (2002)

12. J. C. Miller and R. F. Haglund, Jr., eds., *Laser Ablation and Desorption* (Academic, New York, 1998)
13. R.E. Russo, X.L. Mao, and O.V. Borisov, *Trends in Analytical Chemistry*, **17**, 461 (1998)
14. H. Sankur and J.T. Cheung, *Appl. Phys. A*, **47**, 271 (1988)
15. J. J. Ritsko, in *Laser Micro-Fabrication: Thin Film Processes and Lithography*, eds. D. J. Ehrlich and J. Y. Tsao (Academic, San Diego, 1989)
16. A.A. Oraevsky, R.O. Esenaliev, and V.S. Letokhov, Pulsed laser ablation of biological tissue: Review of the mechanism, in *Laser ablation: mechanisms and applications*, edited by J.C. Miller and R.F. Haglund, Jr. (Springer, New York, 1991)
17. P. Fichet, P. Mauchien, J.F. Wagner and C. Moulin, *Anal.Chim.Acta* **429**, 269 (2001)
18. R.Barbini, F. Colao, R. Fantoni, A. Palucci and F. Capitelli, *Appl. Phys. A* **69**, S175 (1999)
19. Y. Yoon, T. Kim, M. Yang, K.Lee and G. Lee, *Microchem. J.* **68**, 251 (2001)
20. O. Samek, D. C. S. Beddows, H. H. Telle, G. W. Morris, M. Liska and J. Kaiser, *Appl. Phys. A* **69**, S179 (1999)
21. H. S. Kwok, P. Mattocks, L. Shi, X. W. Wang, S. Witanachchi, Q. Y. Ying, J. P. Zheng and D. T. Shaw, *Appl. Phys. Lett.*, **52**, 1825 (1988)
22. M. Lenzner, F. Krausz, J. Kruger and W. Kautek, *Applied Surface Science* **154-155**, 11 (2000)

23. P. Rudolph, J. Bonse, J. Kruger and W. Kautek, *Applied Physics A* **69**, S763 (1999)
24. B. Le Drogoff, J. Margot, M. Chaker, M. Sabsabi, O. Barthelemy, T.W. Johnston, S. Laville, F. Vidal and Y. von Kaenel, *Spectrochim. Acta Part B* **56**, 987 (2001)
25. R.E. Russo, X. Mao and S.S. Mao, *Analytical Chemistry* **74**, 70A (2002)
26. S.S. Mao, X.L. Mao, R. Greif and R.E. Russo, *Appl. Phys. Lett.* **76**, 31 (2000)

Chapter 2

Influence of cavity dimensions on laser-induced plasma properties

2.1 Introduction

Depending on the laser intensity, laser ablation of solids involves processes of heating, melting, vaporization, ejection of atoms, ions and molecules, shock waves, plasma initiation and plasma expansion. The amount of laser energy coupled into a material influences the amount of mass removed, its temperature, phase, and degree of ionization [1]. Many laser-material processes produce cavity structures; e.g. laser drilling, micromachining, and depth resolved chemical analysis [2, 3, 4]. Laser beam energy coupling to a solid was found to increase as a cavity was formed in a target [5, 6]. The increase in energy coupling was related to the cavity depth-to-diameter (aspect) ratio. For an aspect ratio varying from 0 to 5, the amount of energy coupled increased approx 10 times compared to the energy coupled to a flat surface [5].

Elemental depth variations in solid samples are important for micro analytical applications; for example, analysis of inclusion spatial heterogeneity, and elemental diffusion. Previous work [7, 8, 9] showed that the cavity aspect ratio influenced elemental fractionation, a process during which elements are selectively ablated; the ablated mass composition is not the same as the solid. For some elements, fractionation became significant when the cavity aspect ratio was greater than six [7]. Mechanisms to describe the effect of the cavity aspect ratio on

fractionation have not been established. Because the plasma is restricted in the cavity at early times, it may have a larger electron number density and be at a higher temperature compared to a plasma produced at a flat surface. At higher temperatures, the plasma can transfer heat more effectively to the cavity walls. Low melting/vaporization point elements may be selectively removed from the sample by a plasma heating process [7]. As the aspect ratio increases, plasma heating may become the dominant sampling process.

In this chapter, plasma properties were measured inside and outside of prefabricated cavities in fused silica samples. The spatial distribution (up to 1 mm above the target surface) of the plasma temperature and electron number density were determined by measuring the Stark broadening of the Si emission lines and the relative line-continuum ratio at times from 60 to 300 ns after the laser pulse.

2.1 Experimental System

A diagram of the experimental system is shown in Figure 2.1. A 266 nm Nd:YAG laser (Coherent, Infinity) with a 3-ns pulse width was used as the ablation laser. The laser beam was focused vertically onto the sample with a quartz lens to a spot diameter of ~50 microns in air at 1 atm. pressure. The pulse energy was measured using a pyroelectric detector and a joulemeter. A second lens was used to image the laser-induced plasma horizontally onto the entrance slit of a Czerny-Turner spectrometer (Spex Industries Model 270M). Spectral emission was detected by an Intensified Charge-Coupled Device (ICCD) system which consists

of a thermoelectrically cooled CCD (EG&G Princeton Applied Research Model OMA VISION) with 512×512 pixels and a Microchannel Plate (MCP) image intensifier. This detection system provides a spectral window of ~13 nm and resolution of typically 0.125 nm, using an entrance slit width of 20 micron and grating of 1800 grooves/mm. The spatial resolution of the ICCD spectrometer plus lens arrangements was 11 microns per pixel. The dark current background of the CCD detector was subtracted from the measured spectroscopic data for each measurement.

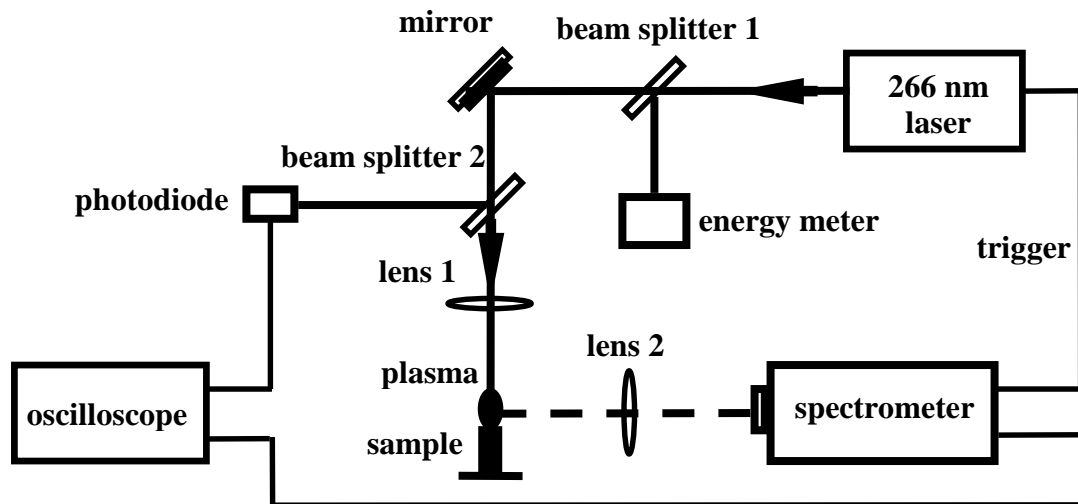


Figure 2.1 Experimental system for spectroscopic measurements of laser-induced plasma.

Gating the ICCD and changing the delay time enables the spectra to be temporally resolved. The gate width and time delay were controlled by the OMA SPEC 4000 software (EG&G Princeton Applied Research), and synchronously triggered from the Nd:YAG laser. A photo diode and a digitizing oscilloscope were used to calibrate the time delay. The gate width was set at 30 ns.

Fused silica was cut into samples of 2 mm width and 2 mm height, and placed on an *xyz* translation stage. Cavities were pre-fabricated using Gaussian beam nanosecond laser ablation, by varying the lens-to-sample distance (spot size), energy, and number of pulses. Three cavities with the same depth of about 0.5 mm, and different diameters were obtained by repetitive laser ablation to produce aspect ratios of 1, 3 and 6 (Figure 2.2). A white-light interferometric microscope (New View 200, Zygo Corporation) and CCD camera system were used to measure the cavity dimensions. All three cavities narrowed towards the bottom, and cavity walls were not smooth due to fracturing. Single pulse laser ablation was performed at the bottom surface of these cavities. The plasma properties measured in the cavities were compared to those from ablation at the flat sample surface. The spot size and energy (fluence) were equal when the laser beam was incident on the flat surface and on the bottom surface of each cavity.

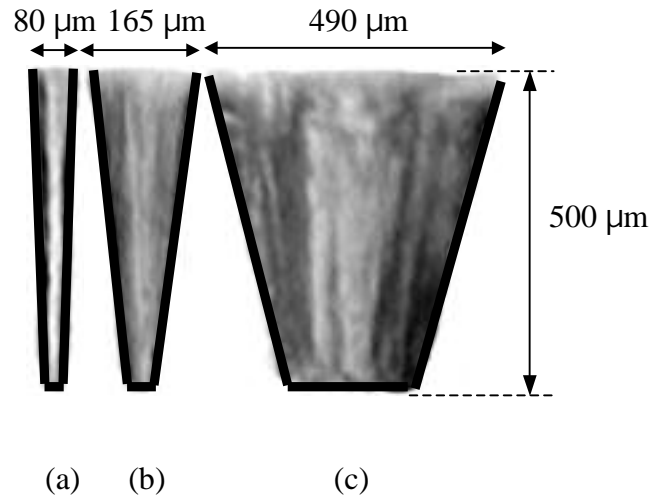


Fig. 2.2 Cavities formed during repetitive laser ablation in fused silica. (a) 80-micron diameter, 480-micron depth cavity formed after 700 pulses laser ablation at an irradiance of 2.9 GW/cm^2 . (b) 165-micron diameter, 485-micron depth cavity formed after 850 pulses laser ablation at an irradiance of 2.1 GW/cm^2 . (c) 490-micron diameter, 480-micron depth cavity formed after 1100 pulses laser ablation at an irradiance of 1.5 GW/cm^2 . The bold lines are schematic cross-sections of the cavities.

2.3 Results and Discussion

2.3.1 Spectral line analysis

The silicon emission line Si(I) at 288.16 nm was measured for diagnosing plasma properties. Figure 2.3a shows the spectra from single pulse laser ablation inside a cavity of 160-micron diameter at 100 ns time delay. The plasma spectra from ablation on a flat surface using the same laser conditions are shown in Figure 2.3b. Inside the cavity, the spectra have a wider Full Width at Half Maximum

(FWHM) and greater emission intensity. The maximum emission intensity from the cavity plasma occurs 0.9 mm above the cavity bottom (0.5 mm depth). The location of maximum emission intensity occurred at 0.6 mm above the flat surface.

Stark line broadening from collisions of charged species is the primary mechanism influencing these emission spectra. The Lorentz function can be used to fit these spectra and is expressed as [10]:

$$y = y_0 + \frac{2A}{\pi} \frac{w}{4(x - x_c)^2 + w^2} \quad (3.1)$$

where w is the full width at half maximum, x_c is the center wavelength, y_0 is the background emission, and A is the integrated area of the emission line. The values of these parameters were obtained by fitting the spectral lines (as shown in Figure 2.4) and were used to deduce the electron number density and temperature of the plasmas.

Other contributions to spectral line broadening were considered. Doppler broadening due to the random thermal motion of the emitters was estimated by using $w_{1/2} = 7.16 \times 10^{-7} \lambda (T / M)^{1/2}$, where M is the atomic weight, T is the plasma temperature in Kelvin, and λ is the line wavelength [11]. As will be shown below, the calculated highest plasma temperature was less than 60,000 K. The calculated Doppler effect will cause a change in line-width for Si(I) 288.16 nm of less than 0.01 nm. Compared with the total line widths (usually about 1 nm), the Doppler effect can be ignored. Resonance broadening is neglected since the atomic Si(I) 288.16 nm line is not a resonance transition [10].

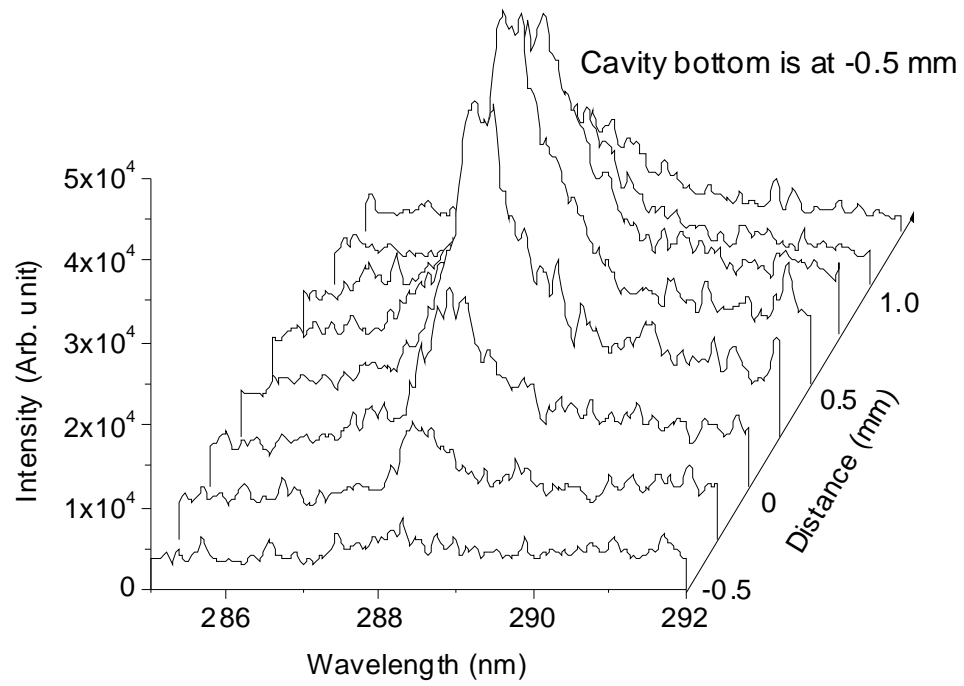


Fig. 2.3 (a) Spatial distributions of plasma emission from the 160-micron diameter cavity (depth 480 micron) in silica at wavelength of Si(I) 288.16 nm and time of 100 ns. Irradiance was 15.9 GW/cm^2 .

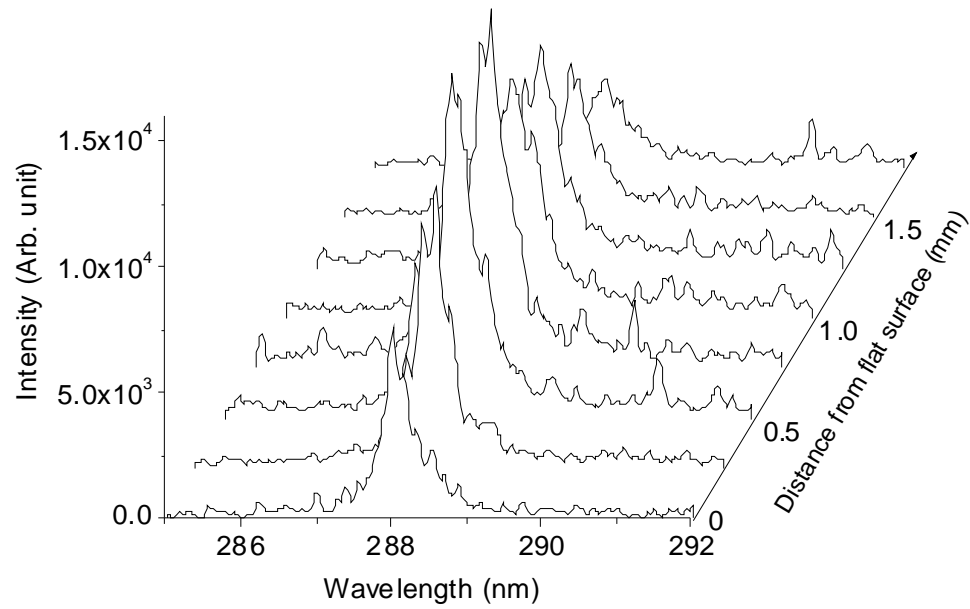


Fig. 2.3 (b) Spatial distributions of plasma emission from the flat surface at wavelength of 288.16 nm and time of 100 ns, irradiance was 15.6 GW/cm^2 .

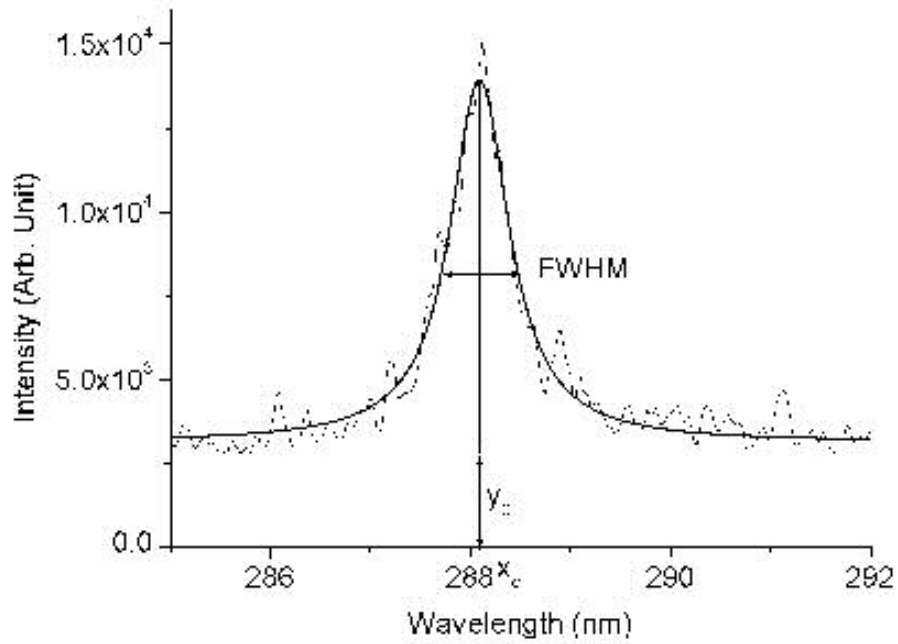


Figure 2.4 Lorentzian fitting of the Stark broadened profile for Si 288.16 nm. The full width half maximum (FWHM) was used for the calculation of the electron number density. The ratio of the integrated spectral line intensity (A) and continuum intensity (y_0) at the center wavelength (x_c) were used for the calculation of plasma temperature.

2.3.2 Electron number densities and Plasma temperature

The FWHM of Stark broadened lines is related to the electron number density n_e by the expression [12]:

$$\Delta\lambda_{1/2} = 2W\left(\frac{n_e}{10^{16}}\right)\left[1 + 1.75A\left(\frac{n_e}{10^{16}}\right)^{1/4}\left(1 - \frac{3}{4}N_D^{-1/3}\right)\right] \quad (2.2)$$

where N_D is the number of particles in the Debye sphere and is estimated from:

$$N_D = 1.72 \times 10^9 \frac{T^{3/2}}{n_e^{1/2}} \quad (2.3)$$

where T is in eV and n_e is in cm^{-3} .

Under the assumption of local thermal equilibrium (LTE), the electron temperature T_e can be assumed equal to the excitation temperature T_{exc} , namely $T_e = T_{exc} = T$. Therefore, the plasma temperature T can be determined by the relative line-to-continuum intensity ratio using the following equation [13]:

$$\frac{\varepsilon_l(\lambda)}{\varepsilon_c} = C_r \frac{A_{21} g_2}{Z_i} \frac{\lambda_c^2}{\lambda_l T_e} \frac{\exp\left(\frac{E_i - E_2 - \Delta E_i}{kT_e}\right)}{\left[\xi \left(1 - \exp\left(\frac{-hc}{\lambda kT_e}\right)\right) + G \left(\exp\left(\frac{-hc}{\lambda kT_e}\right)\right) \right]} \quad (2.4)$$

where ε_c is the continuum emission coefficient and ε_l is the integrated emission coefficient over the line spectral profile. The ratio $\varepsilon_c/\varepsilon_l$ can be calculated from the integrated line intensity and continuum intensity at certain adjacent wavelength positions. λ_c , λ_l are the continuum and center wavelength of the spectral line, respectively. By using a Lorentz fit, the position was obtained, so $\lambda_l = \lambda_c$. Z_i is the partition function for ions, and must be calculated as a function of temperature. A_{21} is the Einstein transition probability of spontaneous emission, and E_i is the ionization potential. E_2 and g_2 are upper level energy and degeneracy, respectively. ΔE_i is the lowering of the ionization potential of atoms in the presence of a field of ions and is small enough to be neglected. G is the free-free Gaunt factor, and ξ is

the free-bound continuum correction factor. The parameters used for T_e and n_e are listed in Table 1 [14, 15].

Table 1. The parameters used for plasma temperature and electron number density calculations

$A_{21}(10^8 s^{-1})$	g_2	$E_2(eV)$	$E_i(eV)$	ξ	G	$W(nm)$	A	$C_r(sK)$
1.9	3	5.028	8.151	1.4	1	0.848×10^{-3} [14]	0.027	2.005×10^{-5}

The partition function is given by [16]:

$$Z(T) = \sum_i g_i \exp\left(-\frac{E_i}{kT}\right) \quad (2.5)$$

where g_i is the degeneracy or statistical weight of the i -th energy level E_i .

$$g_i = 2J_i + 1 \quad (2.6)$$

and J_i is the angular momentum quantum number of the level. E_i and J_i values were obtained from the NIST data bank [17]. The partition function of singly-charged silicon ions was calculated for the temperature interval from 6,000 to 60,000 K and was approximated by a fifth-order polynomial:

$$Z(T) = 5.33707 + 1.05984Y - 0.87284Y^2 + 0.32479Y^3 + 0.02802Y^4 - 0.00578Y^5 \quad (2.7)$$

where $Y = T \times 10^{-4}$ K. The calculated partition function values agree with those reported in ref. 18 to within 0.5% for temperatures between 6000 and 12000 K (greatest temperature range available in literatures).

The lower limit for the electron number density needed to collisionally maintain the energy-level populations to within 10% of LTE while competing with radiative decay is [10, 19, 20]:

$$n_e (\text{cm}^{-3}) \geq 1.4 \times 10^{14} (kT)^{1/2} \Delta E^3 \quad (2.8)$$

where T is the temperature and ΔE is the energy difference between the upper and lower states. For the Si(I) transition at 288.16 nm, $\Delta E = 4.3$ eV, and at the highest temperature $kT = 4.9$ eV, the lower limit for n_e is $2.5 \times 10^{16} \text{ cm}^{-3}$, which is approximately two orders of magnitude lower than the value of n_e deduced from Stark broadening. Therefore, the validity of the LTE assumption is supported.

Using the Saha equation and the calculated electron number density, the first ionization level of Si will be dominant when the plasma temperature is less than 2.5 eV. When the plasma temperature is greater, ionization will shift toward higher levels and electron collisions with higher ionization states will contribute to continuum radiation, the temperature calculated from Eq. (2.4) may be greater than the accurate plasma temperature.

2.3.3 Effect of cavity aspect ratio

Single pulse ablation was performed in the three cavities and at the flat surface of the sample; data are shown in Figure 2.5a (plasma temperature) and Figure 2.5b (electron number density) for a delay time of 100 ns.

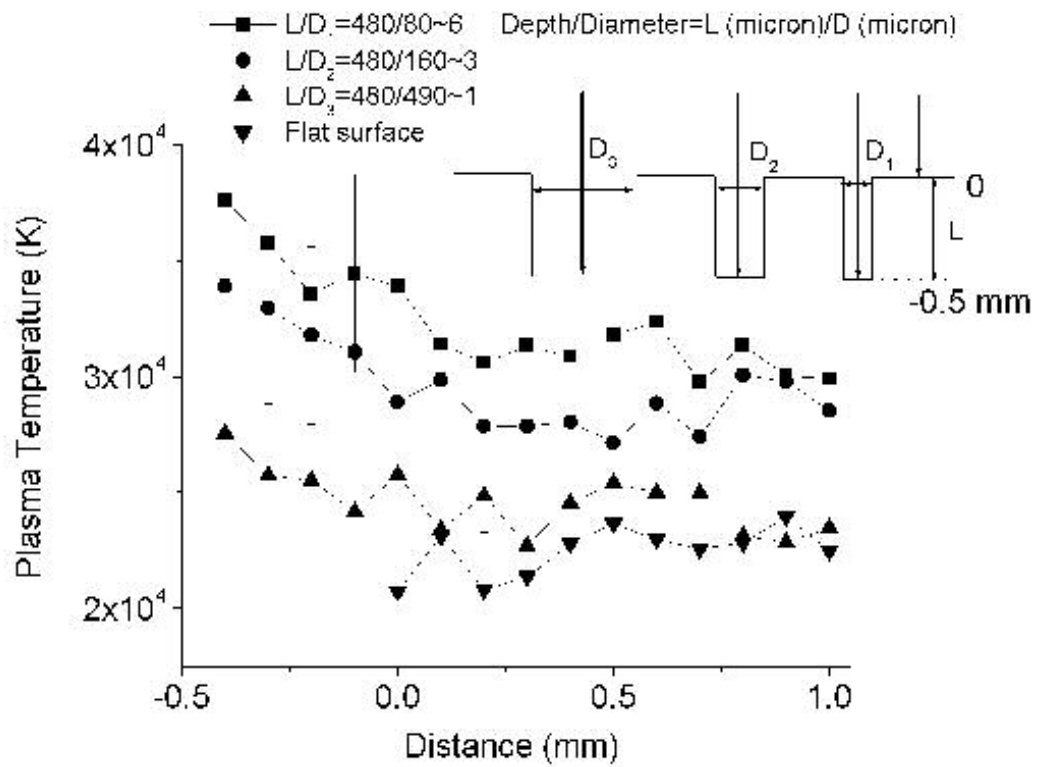


Figure 2.5 (a) Plasma temperature vs. distance from surface. Compare effect of diameter at time of 100 ns and an irradiance of 6.95 GW/cm^2 .

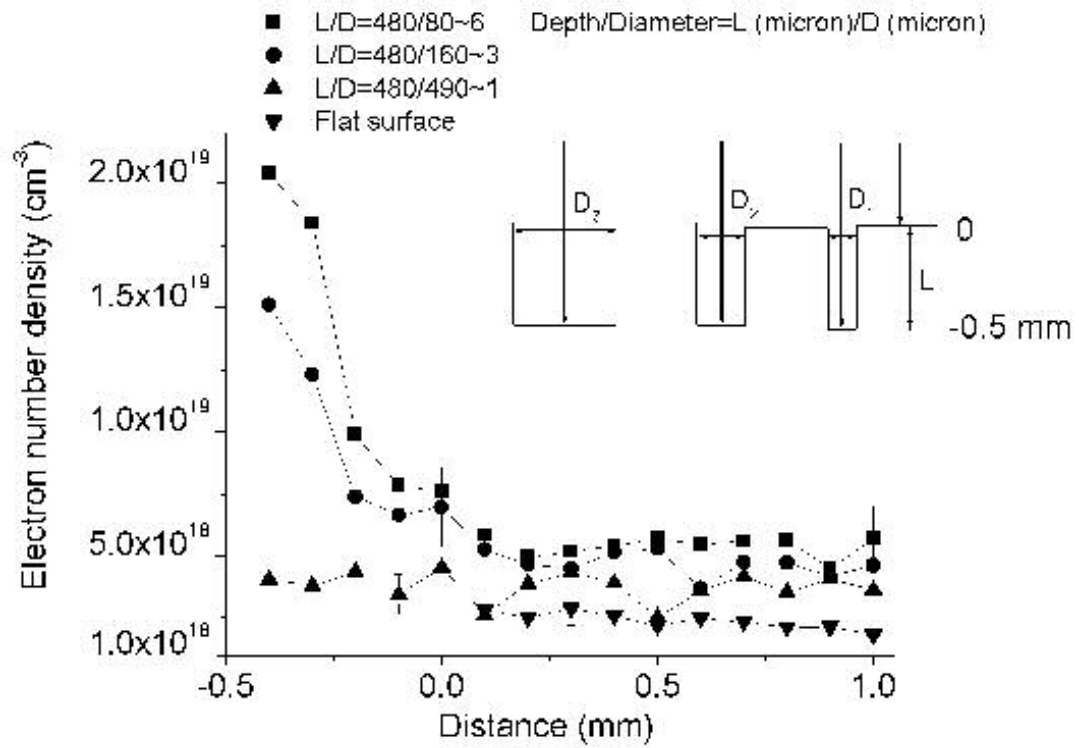


Fig. 2.5 (b) electron number density vs. distance from surface. Compare effect of diameter at time of 100 ns and an irradiance of 6.95 GW/cm².

The plasma temperature and electron number density are greatest in the largest aspect-ratio cavity. As the aspect ratio decreases, the plasma temperature and electron number density in the cavity approach the flat surface condition. For the largest aspect ratio, the plasma temperature decreases from 38000 K (in the cavity) to 30000 K (1.5 mm above the cavity bottom); electron number density falls from 2×10^{19} to $5 \times 10^{18} \text{ cm}^{-3}$. On a flat surface, the plasma temperature and electron number density are much lower, 20000 K and $2 \times 10^{18} \text{ cm}^{-3}$, respectively, and do not change as much with distance from the surface.

Overall, the temperature and electron number density are greater for laser ablation in a cavity compared to flat surface ablation. Comparing the data at 0.2mm above the cavity bottom with the data at 0.2mm above flat surface, n_e is $\sim 10X$ and T is only $\sim 2X$ in the cavity with aspect ratio of 6. These results are believed to be related to reflection and confinement effects by the cavity walls and plasma shielding (absorption and/or reflection of the laser beam by the plasma). Once the plasma is initiated in the cavity, its lateral expansion is confined; electron number density increases greatly, leading to enhanced absorbing of the trailing part of the laser pulse. Additional electrons will be produced via electron-neutral, electron-ion inverse bremsstrahlung, and photoionization [21]. The absorbed energy is converted into internal energy of the plasma. Since the plasma temperature is much higher than the surrounding wall temperature, its internal energy decreases quickly by radiation and other methods. Thus, at 100 ns, plasma temperature is only $\sim 2X$ in the cavity compared with $\sim 10X$ electron number density. Increased plasma

temperature and electron number density in cavities has been reported [8, 9]. Jeong, et al. [6] reported an increase in coupled laser-beam energy by multiple-reflections of the cavity walls utilizing a photothermal deflection measurement technique. Shannon's [5] radiative cavity analysis demonstrated that energy coupling in a cavity increased with increasing aspect ratio, consistent with the data measured here.

2.3.4 Temporal evolution of plasma properties

Figure 2.6 shows the spatial plasma temperature and electron number density inside and outside of a cavity and for the flat surface at three different times, 100, 150 and 265 ns. Both plasma temperature and electron number density are higher inside the cavity than outside the cavity at times of 100 and 150 ns. However, at 265 ns, the electron number density inside the cavity drops below the value outside the cavity, and the plasma temperature inside the cavity approaches the plasma temperature outside the cavity. The plasma temperature and electron number density decrease with time for both the cavity and flat surface. However, the plasma temperature and electron number density in the cavity decrease at a faster rate than for the plasma outside of the cavity and on the flat surface, especially during early times ($t = 100\sim 150$ ns).

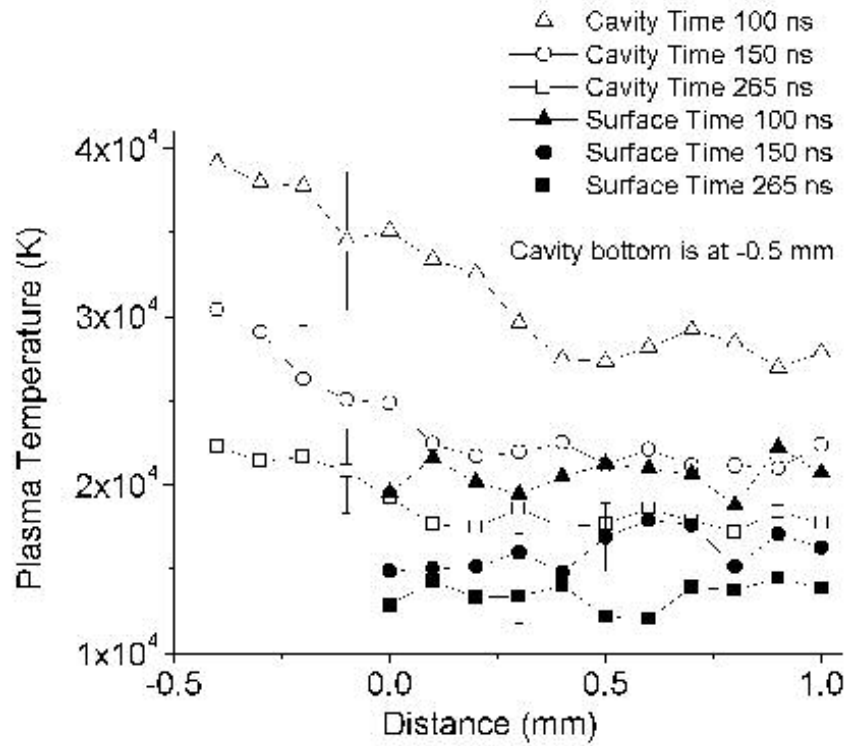


Figure 2.6 (a) Temporal evolution of plasma temperature vs. distance from surface. Compare cavity (Diameter 85 micron, depth 500 micron) and flat surface ablation results, irradiance is 7.95 GW/cm^2 .

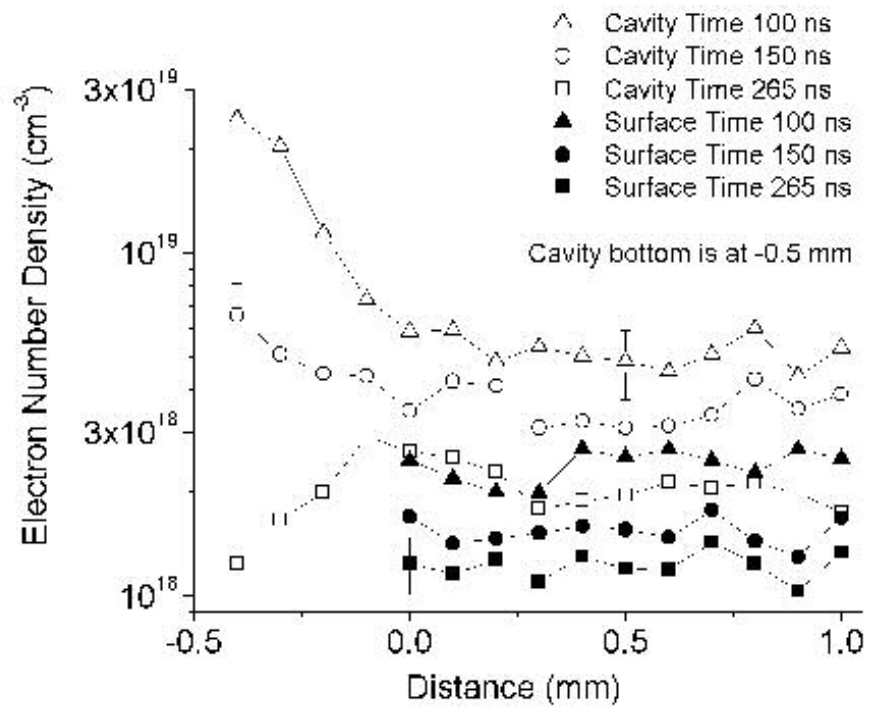


Fig. 2.6 (b) Temporal evolution of electron number density vs. distance from surface. Compare cavity (Diameter 85 micron, depth 500 micron) and flat surface ablation results, irradiance is 7.95 GW/cm^2 .

To compare the temporal evolution of the plasmas, we selected two locations for the cavity and one location for the flat surface (Figure 2.7). Location A is inside the cavity at a height 0.2 mm above the bottom surface, location B is outside of the cavity at a height 0.7 mm above the bottom of the cavity. Location C is 0.2 mm above the flat surface. Location A and C are equal distance above solid material.

The plasma temperature and electron number density in the cavity at location A are higher than both outside the cavity at location B and for the flat surface at location C. Plasma temperature and electron number density in the cavity (A) decrease faster than both outside of the cavity (B) and from the flat surface (C). As the plasma expands there is a sharp decrease of the temperature and electron number density inside the cavity at A. Outside of the cavity, the temperature and electron number density at B decrease at a similar rate to the plasma from the flat surface generated at C.

An adiabatic model is often used to describe laser-induced plasma expansion [21, 22, 23]. For an adiabatic expansion, the expressions for plasma temperature and electron number density as a function of time are: [10, 21]

$$T(t) \propto t^{-2\alpha(\gamma-1)/[\alpha(\gamma-1)+2]}, \quad n_e(t) \propto t^{-2\alpha/[\alpha(\gamma-1)+2]} \quad (2.9)$$

where γ is the ratio of specific heat capacities at constant pressure to constant volume, and α is the flow dimensionality: $1 < \alpha < 3$ [21, 22, 23].

The plasma at location C from laser ablation on the flat surface gives:

$$T \propto t^{-0.54 \pm 0.04}, \quad n_e \propto t^{-0.95 \pm 0.06} \quad (2.10)$$

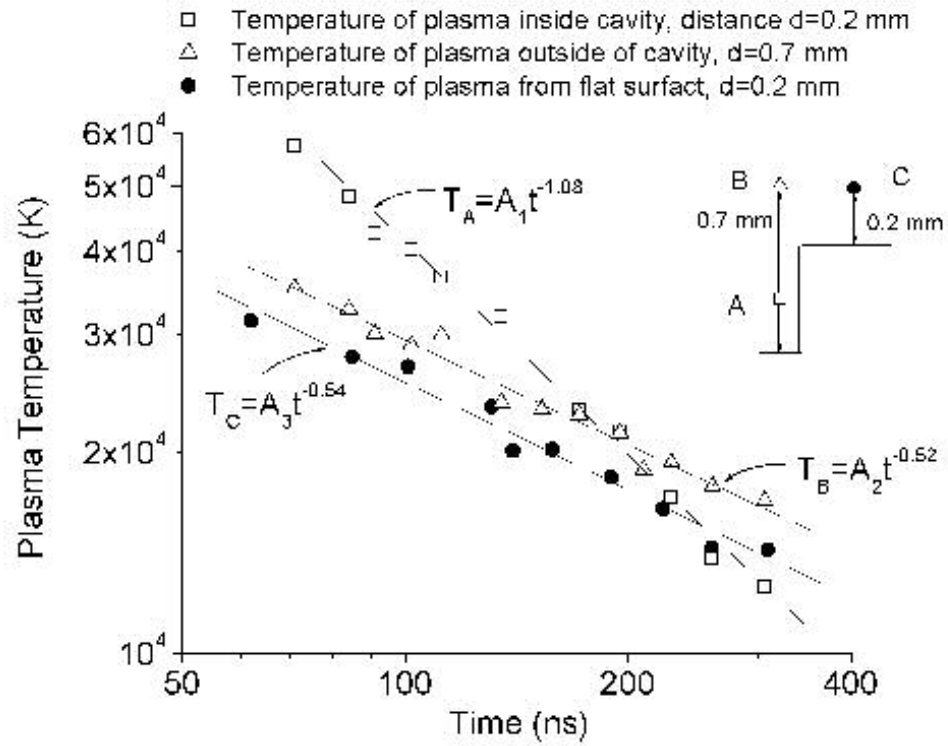


Figure 2.7 (a) Temporal evolution of plasma temperature inside and outside of the cavity. Cavity diameter is 80 micron and depth 480 micron. Irradiance is 7.67 GW/cm².

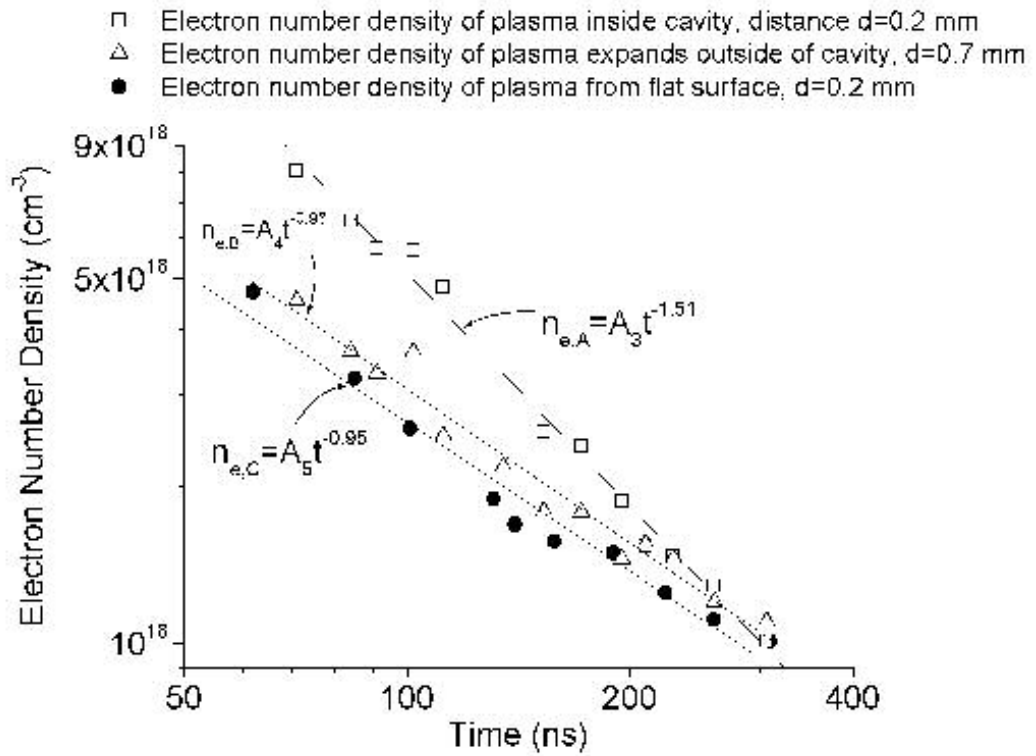


Figure 2.7 (b) Temporal evolution of electron number densities inside and outside of the cavity. Cavity diameter is 80 micron and depth 480 micron. Irradiance is 7.67 GW/cm^2 .

Solving for α and γ yields:

$$\alpha = 1.30 \pm 0.12, \gamma = 1.57 \pm 0.08 \quad (2.11)$$

The calculated values of α and γ are within experimental error to the values obtained by Liu, et al. [10]. The calculated dimensionality 1.30 supports preferential spatial expansion in the direction perpendicular to the target [21, 22, 23]. The calculated γ value, 1.57 is close to the specific heat for an ideal gas of 5/3. Therefore, an adiabatic process can be used to describe the plasma expansion for this experiment.

Plasma expansion outside the cavity at location B gives:

$$T \propto t^{-0.52 \pm 0.03}, n_e \propto t^{-0.98 \pm 0.05} \quad (2.12)$$

From equations (9) and (12),

$$\alpha = 1.32 \pm 0.09, \gamma = 1.53 \pm 0.06 \quad (2.13)$$

which are close to the flat surface results above. Thus, after the plasma expands out of the cavity, an adiabatic model can describe plasma temperature and electron number density variations.

For the plasma in the cavity at A,

$$T \propto t^{-1.08 \pm 0.04}, n_e \propto t^{-1.51 \pm 0.06} \quad (2.14)$$

Therefore,

$$\alpha = 3.31 \pm 0.17, \gamma = 1.72 \pm 0.05 \quad (2.15)$$

The dimensionality value is greater than 3 (3-Dimension expansion), which indicates that an adiabatic expansion model is not suitable for the laser-induced plasma in a cavity. To describe the processes of a laser-induced plasma in cavity

and account for the sharp decrease of plasma temperature and electron number density (cf. Figures 6a, 6b), plasma wall interactions should be included in the expansion model analysis. Energy from the plasma can be transferred to the wall by any of the four mechanisms: (1) normal electron heat conduction, (2) electron-ion (exothermic) recombination on the cavity walls, (3) short-wavelength thermal plasma radiation, and (4) condensation of vapor that moves to the surface due to the plasma pressure [2].

2.4 Conclusions

The formation of a laser-induced plasma inside a cavity and the cavity effects on plasma expansion were investigated. The temperature and electron number density of a laser-induced plasma inside a cavity were greater than outside of a cavity. When the aspect ratio was six, the plasma temperature inside the cavity was twice that for flat surface ablation and the electron number density was a factor of 10X greater. As the aspect ratio decreased, the plasma temperature in the cavity approached the surface results. Plasma wall interactions must be considered to describe the plasma in the cavity and explain the sharp decrease of plasma temperature and electron number density inside the cavity. As time increased, the plasma temperature and electron number density inside the cavity decreased faster than outside of the cavity; an adiabatic model was not suitable to describe the plasma in the cavity because plasma wall interactions were not included.

REFERENCE

1. J.F. Ready, Effects of High-Power Laser Radiation (Academic, New York, 1971)
2. M.V. Allmen, Laser-beam Interactions with Materials (Springer-Verlag, New York, 1987)
3. E. N. Sobol, Phase Transformations and Ablation in Laser-Treated Solids (John Wiley & Sons, New York, 1995)
4. L. W. Boyd, Laser Processing of Thin Films and Microstructures (Springer-Verlag, New York, 1987)
5. M. A. Shannon, Applied Surface Science, **127-129**, 218 (1998)
6. S. H. Jeong, J. Appl. Phys. **80**, 1996 (1996)
7. A.J.G. Mank, P.D. Mason, J. Anal.At.Spectrom. **14**, 1143 (1999)
8. O.V. Borisov, X. Mao, R. E., Russo, Spectrochim. Acta Part B **55**, 1693 (2000)
9. S.M. Eggins, L.P.J. Kinsley, J.M.G. Shelley, Appl.Surf.Sci. **127-129**, 278 (1998)
10. H.C. Liu, X.L. Mao, J.H. Yoo, R.E. Russo, Spectrochim. Acta Part B **54**, 1607 (1999)
11. M. Miller, in: A. Montaser, D.W. Golightly (Eds.), Inductively Coupled Plasmas in Analytical Atomic Spectrometry (VCH Publishers Inc, New York, 1987)
12. G. Befeki, Principles of laser plasmas (Wiley Interscience, New York, 1976)
13. G.J. Bastiaans, R.A. Mangold, Spectrochim.Acta, Part B **40B**, 885 (1985)

14. H.R. Griem, Spectral Line Broadening by Plasmas (Academic, New York, 1974)
15. L. Spitzer, Physics of Fully Ionized Gases (John Wiley & Sons, New York, 1962)
16. H.R. Griem, Plasma Spectroscopy (McGraw-Hill, New York, 1964)
17. Atomic Spectra Databases. Version 2.0. National Institute of Standards and Technology (NIST), USA, 1999. (<http://www.nist.gov>).
18. S. Tamaki, T. Kuroda, Spectrochimica Acta, **42B**, 1105 (1987)
19. P.J. Wolf, J.Appl.Phys. **72**, 1280 (1992)
20. R.W.P. McWhirter, in: R.H. Huddlestone and S.L. Leonard (Eds.), Plasma Diagnostic Techniques (Academic, New York, 1965)
21. C.R. Phipps, R.W. Dreyfus, in: A. Vertes, R. Gijbels, F. Adams (Eds.), Laser Ionization Mass Analysis (John Wiley & Son, New York, 1993)
22. R.K. Singh, J. Narayan, Phys. Rev. B **41**, 8843 (1990)
23. R.K. Singh, O.W. Holland, J. Narayan, J. Appl. Phys. **68**, 233 (1998)

Chapter 3

Dependence of Properties of Laser-Induced Plasma in a Cavity on Laser Irradiance

3.1 Introduction

In chapter two, the laser induced plasma in a cavity was found to have a larger electron number density and to be at a higher temperature compared to a plasma produced on a flat surface. In this chapter, the influence of crater formation on the plasma characteristics at different laser energy levels was investigated.

The amount of laser energy absorbed by a material influences the amount of mass removed, its temperature, phase, and degree of ionization in the plasma [1]. Jeong, et al. [2] reported an increase in coupled laser-beam energy by multiple-reflections of the cavity walls, utilizing a photothermal deflection technique to measure the refractive index change of the ambient medium adjacent to the sample.

With increasing laser irradiance, a dramatic change in the plasma characteristics and a sharp increase of mass removal were observed using high power nanosecond lasers and silicon samples [3, 4]. The threshold irradiance was about 20 GW/cm^2 . Explosive boiling was proposed to explain these changes. Since energy coupling and plasma properties are related to the cavity aspect ratio, it is of interest to study how the threshold irradiance of explosive boiling is influenced by the cavity aspect ratio.

In this chapter, plasma properties were measured at different laser irradiances for laser ablation in fused silica cavities with different aspect ratios and

compared to flat surface data. The irradiance range was 2 – 40 GW/cm². The spatial distribution (from the bottom of the cavity to a height 1 mm above the target surface) of the plasma temperature and electron number density were determined by measuring the Stark broadening of the Si emission lines and the relative line-continuum ratio at a time of 30 ns after the laser pulse.

3.2 Experimental System

The experimental setup for spectroscopic measurements of plasma properties has been described in chapter 2 (Figure 2.1). Briefly, A 266 nm Nd:YAG laser with a 3-ns pulse width was used as the ablation laser. A Czerny-Turner spectrometer was used to measure the silicon emission line Si(I) at 288.16 nm for diagnosing plasma properties.

Two cavities with the same depth of about 0.5 mm, but different diameters (130 micron, 250 micron) were fabricated with aspect ratios of 2 and 4. A white-light interferometric microscope (New View 200, Zygo Corporation) and CCD camera system were used to measure the exact cavity dimensions. Single pulse laser ablation at different laser energies was subsequently performed at the bottom surface of the cavities. The plasma properties were measured in the cavities (spectra were obtained from emission passing through the transparent cavity walls) and were compared to those from ablation at the flat sample. The spot size (fluence) was equal when the laser beam was incident on the flat surface and on the bottom surface of each cavity.

3.3 Results and Discussion

The typical spectral lines from ablation inside a cavity versus a flat surface are shown in Figure 3.1. The spectral lines were measured at a distance of 1 mm above the surface (either original flat surface or bottom of cavity), the peak position of plasma emission intensity. The line shape was found to best fit a Lorentzian function, indicating self-absorption was negligible. For ablation inside the cavity, the spectra had a wider Full Width at Half Maximum (FWHM) and greater emission intensity.

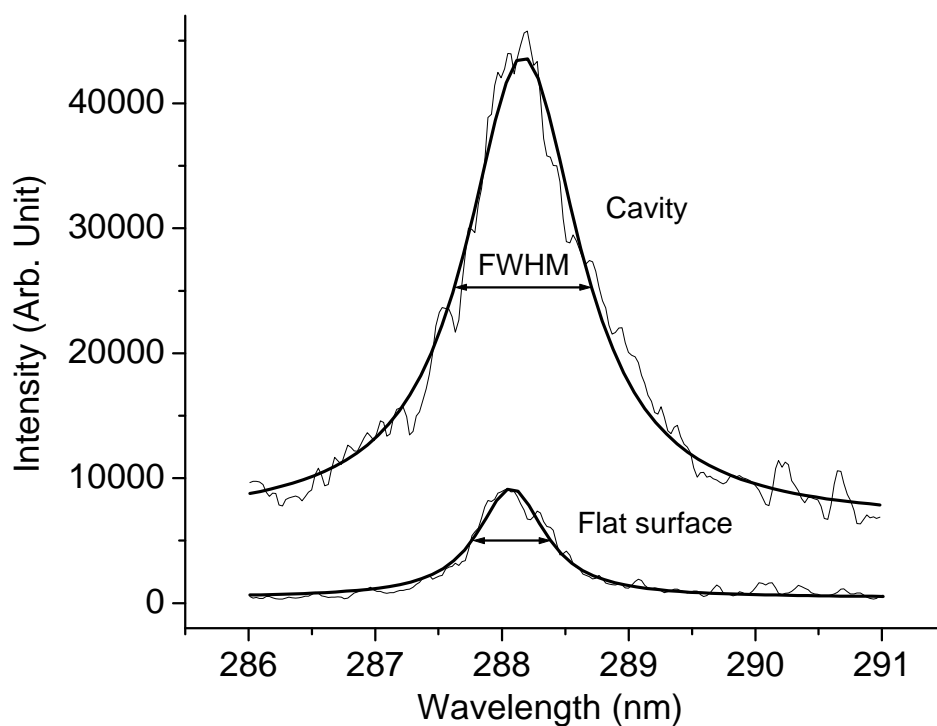


Figure 3.1 Si(I) 288.16 nm spectral line and continuum emission at time of 30 ns, distance of 1 mm and irradiance of 15 GW/cm^2 . Compare flat surface and cavity (Diameter 250 micron, depth 500 micron) ablation results. Bold lines are Lorentzian fitting curves.

3.3.1 Electron number density and plasma temperature calculation: second ionization effects

Under the assumption of local thermal equilibrium (LTE), the plasma temperature T can be determined by the line-to-continuum intensity ratio $\varepsilon_c/\varepsilon_l$, where ε_c is the continuum emission coefficient and ε_l is the integrated emission coefficient over the line spectral profile. In chapter 2, only the first ionization potential of silicon was considered in the spectral analysis. However, as laser intensity and plasma temperature increases, higher ionization levels should be included.

The emission coefficient ε_l can be expressed in terms of the electron temperature and density [5]:

$$\varepsilon_l = \left(\frac{h\nu}{4\pi}\right) A_{21} \frac{g_2}{2Z_{ion}(T)} \frac{h^3}{(2\pi mk)^{3/2}} n_e n_i T_e^{-3/2} \exp\left(\frac{E_{ion} - E_2 - \Delta E_i}{kT_e}\right), \quad (3.1)$$

where A_{21} is the Einstein transition probability of spontaneous emission, and E_{ion} is the ionization potential. E_2 and g_2 are upper level energy and degeneracy, respectively. ΔE_i is the lowering of the ionization potential of atoms in the presence of a field of ions and is small enough to be neglected. $Z_{ion}(T)$ is the partition function for ions, which is given by [6]:

$$Z_{ion}(T) = \sum_i g_i \exp\left(-\frac{E_i}{kT}\right), \quad (3.2)$$

with g_i the degeneracy or statistical weight of the i -th energy level E_i ,

$$g_i = 2J_i + 1, \quad (3.3)$$

where J_i is the angular momentum quantum number of the level. The values of E_i and J_i were obtained from the NIST data bank [7]. The partition functions of silicon atoms, singly-charged and doubly-charged silicon ions were calculated for the temperature interval from 6,000 to 50,000 K. The data were fit with third-, fourth-, and fifth-order polynomials using a least squares method. Each of these fits was then compared to the original data at temperatures of 6000, 25000 and 50000 K. The fifth-order polynomials were selected due to the lowest total error.

$$Z(T) = a + bY + cY^2 + dY^3 + eY^4 + fY^5, \quad (3.4)$$

where $Y = T \times 10^{-4}$ K; a, b, c, d, e and f are given in Table 3.1. The calculated values of the partition function agree with those reported in ref. 8 to within 0.5% for temperatures between 6000 and 12000 K (the largest temperature range available in the literature).

Table 3.1. Coefficients for partition functions of silicon atom, singly-charged and doubly-charged silicon ions (Eq. 3.4)

	a	b	c	d	e	f
Si	14.534	21.9	-58.135	41	-7.8237	0.5011
Si ⁺	4.9632	1.8184	-1.445	0.52732	-0.00596	-0.0036
Si ²⁺	1.3178	-0.61576	0.33364	-0.02366	-0.00367	0.00122

Based on the calculations using Saha equation, and the electron number density measured in this work, the first ionization level of silicon is dominant for

temperatures less than 25000 K. For greater temperatures, the ionization shifts toward higher levels. The doubly charged silicon ions are dominant when the temperature is greater than 40000 K.

By including the second ionization contribution to the continuum radiation, the continuum emission coefficient can be rewritten as [5, 6]:

$$\varepsilon_c = \left(\frac{16\pi e^6}{3c^3 (6\pi m^3 k)^{1/2}} \right) n_e (n_i^+ + 4n_i^{++}) T_e^{-1/2} \left[\xi \left(1 - \exp \frac{-hv}{kT_e} \right) + G \left(\exp \frac{-hv}{kT_e} \right) \right]. \quad (3.5)$$

From equations (3.1) and (3.5), the line to continuum ratio is:

$$\frac{\varepsilon_l}{\varepsilon_c} = \frac{1}{1 + 4 \left(\frac{n_i^{2+}}{n_i^+} \right)} C_r A_{21} \frac{g_2}{Z_{ion}} \frac{\lambda_c^2}{\lambda_l T_e} \frac{\exp \left(\frac{E_i - E_2 - \Delta E_i}{kT_e} \right)}{\left[\xi \left(1 - \exp \left(\frac{-hc}{\lambda k T_e} \right) \right) + G \left(\exp \left(\frac{-hc}{\lambda k T_e} \right) \right) \right]}, \quad (3.6)$$

where Z_{ion} is the partition function for ions. λ_c , λ_l are the continuum and center wavelength of the spectral line, respectively. The center wavelength position was obtained from the Lorentzian fit of the data. The ratio $\varepsilon_c / \varepsilon_l$ can be calculated from the integrated line intensity and continuum intensity at λ_c and λ_l . The parameters used in Eq. (3.6) to determine T_e and n_e from the experimental data are listed in Table 2.1 [9, 10]. The ion ratio $\frac{n_i^{++}}{n_i^+}$ can be calculated from equation (3.7) in the following ion formation efficiency analysis.

The formation efficiencies of singly and doubly charged ions are calculated using the Saha equation [11]:

$$\frac{M^{++}}{M^+} = \frac{(2\pi m_e kT)^{3/2}}{h^3} \frac{2Z_M^{++}(T)}{Z_M^+(T)} \frac{1}{n_e} \exp\left(-\frac{E_{2,ion}}{kT}\right), \quad (3.7)$$

$$\frac{M^+}{M^0} = \frac{(2\pi m_e kT)^{3/2}}{h^3} \frac{2Z_M^+(T)}{Z_M^0(T)} \frac{1}{n_e} \exp\left(-\frac{E_{1,ion}}{kT}\right), \quad (3.8)$$

and the unit condition:

$$M^0 + M^+ + M^{++} = 1, \quad (3.9)$$

where m_e is the electron mass; h is the Planck constant; k is the Boltzmann constant; $Z_M^0(T)$, $Z_M^+(T)$ and $Z_M^{++}(T)$ are the partition functions at the temperature T for an atom, M^+ and M^{++} ions of an element M , respectively. $E_{1,ion}$ and $E_{2,ion}$ are the first and second ionization potentials, respectively.

In Eq. (3.6), the second ionization potential of Si is considered for calculating the plasma temperature. Based on the Saha equation, at higher plasma temperatures, ionization will shift towards even higher levels and electron collisions with the higher ionization states will contribute to continuum radiation. Thus, the temperature calculated from Eq. (3.6) may be greater than the actual plasma temperature.

Stark line broadening from collisions of charged species is the primary mechanism influencing the emission spectra in these experiments. The FWHM of Stark broadened lines is related to the electron number density n_e by Eq. (3.10): [3]

$$\Delta\lambda_{1/2} = 2W\left(\frac{n_e}{10^{16}}\right) \left[1 + 1.75A\left(\frac{n_e}{10^{16}}\right)^{1/4} \left(1 - \frac{3}{4}N_D^{-1/3}\right) \right], \quad (3.10)$$

where N_D is the number of particles in the Debye sphere and is estimated from

$$N_D = 1.72 \times 10^9 \frac{T^{3/2}}{n_e^{1/2}} \quad (3.11)$$

W is the electron impact parameter in nm and A is the ion impact parameter; W and A are functions of temperature and are approximated by second-order polynomials [9]:

$$W(T) = 4.8767 \times 10^{-4} + 1.6385 \times 10^{-8} T - 1.8473 \times 10^{-13} T^2, \quad (3.12)$$

$$A(T) = 0.03983 - 7.0226 \times 10^{-7} T + 9.5699 \times 10^{-12} T^2. \quad (3.13)$$

A Lorentz function was used to fit the spectra. The FWHM of Stark broadened lines and the line to continuum emission ratio were used to deduce the electron number density and temperature of the plasmas using equations (3.6) and (3.10).

3.3.2 Effect of laser energy on formation of a plasma inside a cavity

Laser-sample and laser-plasma interactions are strongly dependent on the laser beam irradiance on the target. The plasma temperatures and electron number densities for laser ablation inside cavities and on a flat surface as a function of laser irradiance are shown in Figure 3.2. The data were measured at a delay time 30 ns and at a distance of 1mm above the target. The electron number density and plasma temperature are greater at each irradiance as the cavity aspect ratio increases. For the flat surface, the electron number density and plasma temperature change dramatically at a threshold value of $\sim 20 \text{ GW/cm}^2$. The threshold irradiance is lower for laser ablation in a fused silica cavity compared with a flat surface; the

greater the cavity aspect ratio, the lower the threshold irradiance. For the aspect ratio of 2 cavity, the threshold value is $\sim 9 \text{ GW/cm}^2$; for the aspect ratio of 4 cavity, the threshold value is $\sim 5 \text{ GW/cm}^2$.

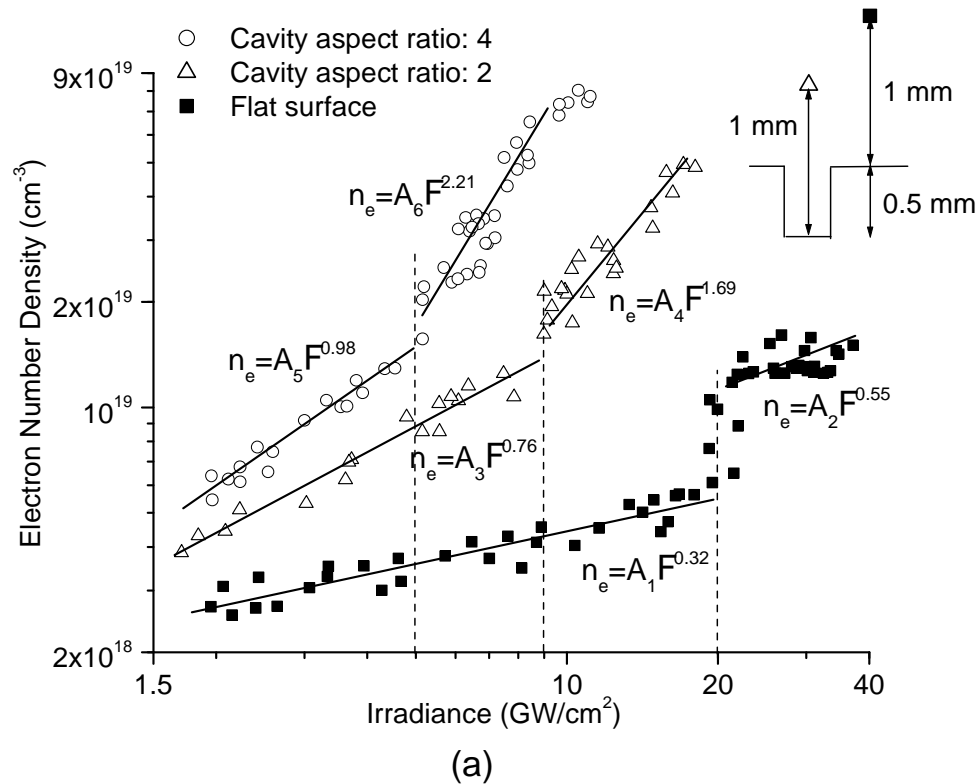


Figure 3.2 (a) Electron number density vs. irradiance. Compare flat surface and two cavity (Diameter 130 micron, depth 500 micron, aspect ratio 4; Diameter 250 micron, depth 500 micron, aspect ratio 2) ablation results at time of 30 ns and distance of 1mm. Sample was fused silica.

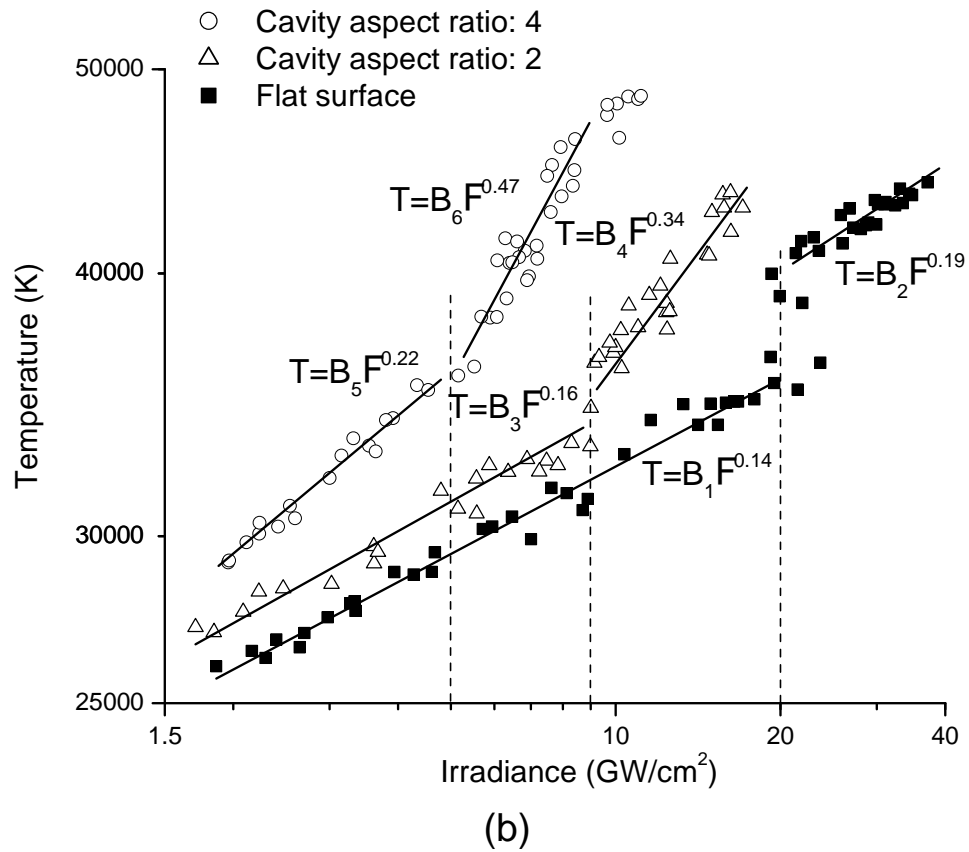


Figure 3.2 (b) plasma temperature vs. irradiance. Compare flat surface and two cavity (Diameter 130 micron, depth 500 micron, aspect ratio 4; Diameter 250 micron, depth 500 micron, aspect ratio 2) ablation results at time of 30 ns and distance of 1mm. Sample was fused silica.

In the irradiance regions lower and higher than the threshold, the electron number density and plasma temperature increase faster with irradiance as the cavity aspect ratio increases. These data are related to confinement and reflection effects by the cavity walls and plasma shielding as discussed in chapter 2.

The spatial distributions of plasma temperature and electron number density for laser ablation inside a cavity and on a flat surface below and above the threshold irradiance at a time of 30 ns are shown in Figure 3. Below the threshold irradiance, the electron number densities do not change significantly with distance for both cavity and flat surface results (Figures 3.3a and 3.3c). However, when the irradiances were greater than the threshold, the electron number densities exhibit a peak profile centered at about 0.5 mm from the surface. The maximum electron number density was about two times greater than the electron number densities below the threshold irradiance, while the irradiance increased only 23% for the flat surface results. For cavity results, the maximum electron number density was about three times greater with 50% increase of the irradiance. Plasma temperature also increased significantly after the threshold irradiances for both cavity and flat surface results (Figures 3.3b and 3.3d). Due to heat transfer from the plasma to the cavity walls, plasma temperature decreases more rapidly as it expands from inside the cavity (Figure 3.3d).

Figure 3.4 shows the variation of the Si^+ and Si^{2+} formation efficiency versus laser irradiance. After the irradiance reaches the threshold, ionization becomes saturated for both the cavity and flat surface.

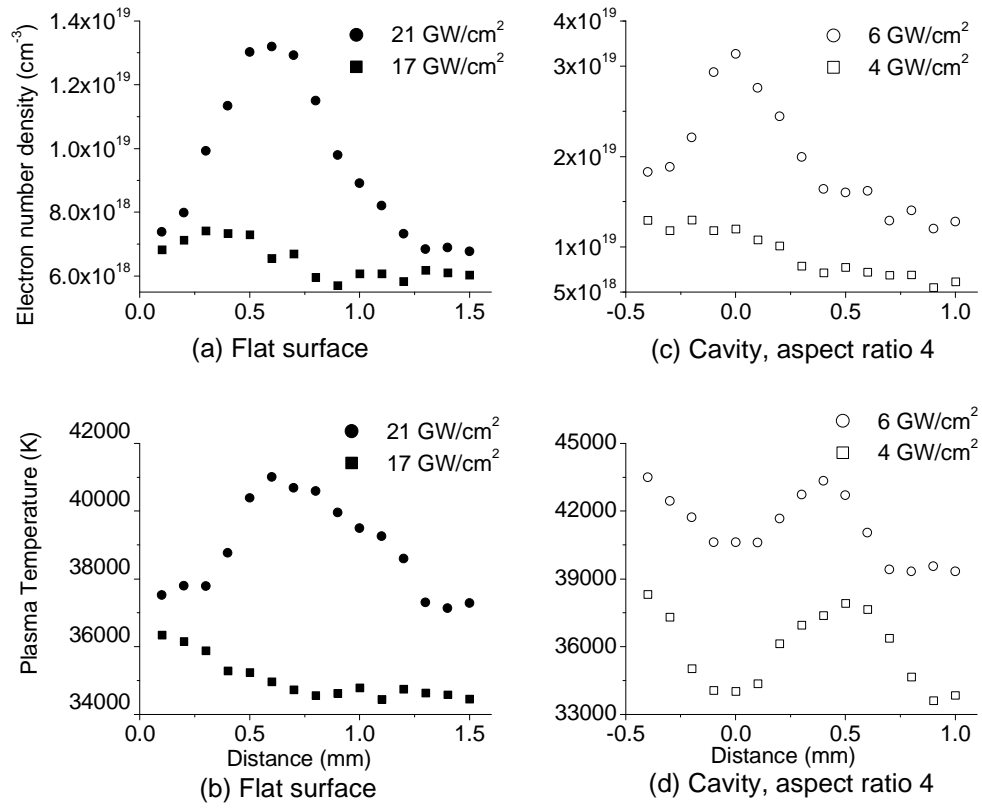


Figure 3.3 Electron number density and plasma temperature vs. distance from surface at below and above threshold irradiances. Compare (a, b) flat surface and (c, d) cavity (Diameter 130 micron, depth 500 micron) ablation results at time of 30 ns.

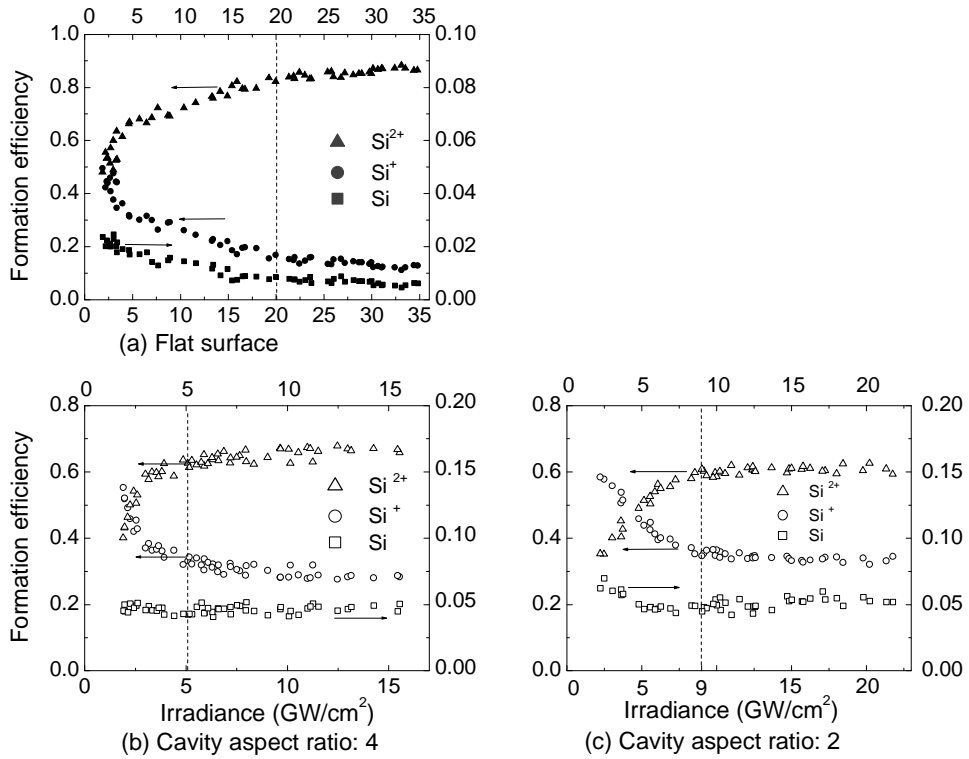


Figure 3.4 Silicon ionization efficiency vs. irradiance. Compare (a) flat surface and two cavity ((b) Diameter 130 micron, depth 500 micron, aspect ratio 4; (c) Diameter 250 micron, depth 500 micron, aspect ratio 2) ablation results at time of 30 ns and distance of 1 mm.

Once the plasma is initiated, absorption of laser radiation generally commences via electron-neutral inverse bremsstrahlung and photoionization of excited state atoms. However, when sufficient ionization is reached (>1%), the dominant laser absorption mechanism changes to electron-ion inverse bremsstrahlung, which involves the absorption of a photon by a free electron during electron-ion collisions. As shown in Figure 3.4, the plasma is significantly ionized when the irradiance is greater than 1 GW/cm², ion density is much greater than the neutral atom density and the electron-ion inverse bremsstrahlung should dominate the absorption. The absorption coefficient α_p (cm⁻¹) for electron-ion inverse bremsstrahlung can be written as [12]:

$$\alpha_p = (3.69 \times 10^8) \frac{Z^3 n_i^2}{T^{1/2} \nu^3} [1 - \exp(-h\nu/kT)], \quad (3.14)$$

where Z , n_i and T are, respectively, the average ion charge state, ion density, and temperature of the plasma. ν is the frequency of the laser light.

Assuming the plasma is in charge equilibrium, the average ion charge state and ion density are calculated from the electron number density and Si^+ , Si^{++} formation efficiencies. Figure 3.5 shows the calculated electron-ion inverse bremsstrahlung absorption coefficient vs. irradiance at a delay time of 30ns. For both cavity and flat surface, the absorption coefficient increased dramatically when the irradiance reached the threshold; e.g., for the flat surface a value of about four times greater than the absorption coefficient below the threshold irradiance.

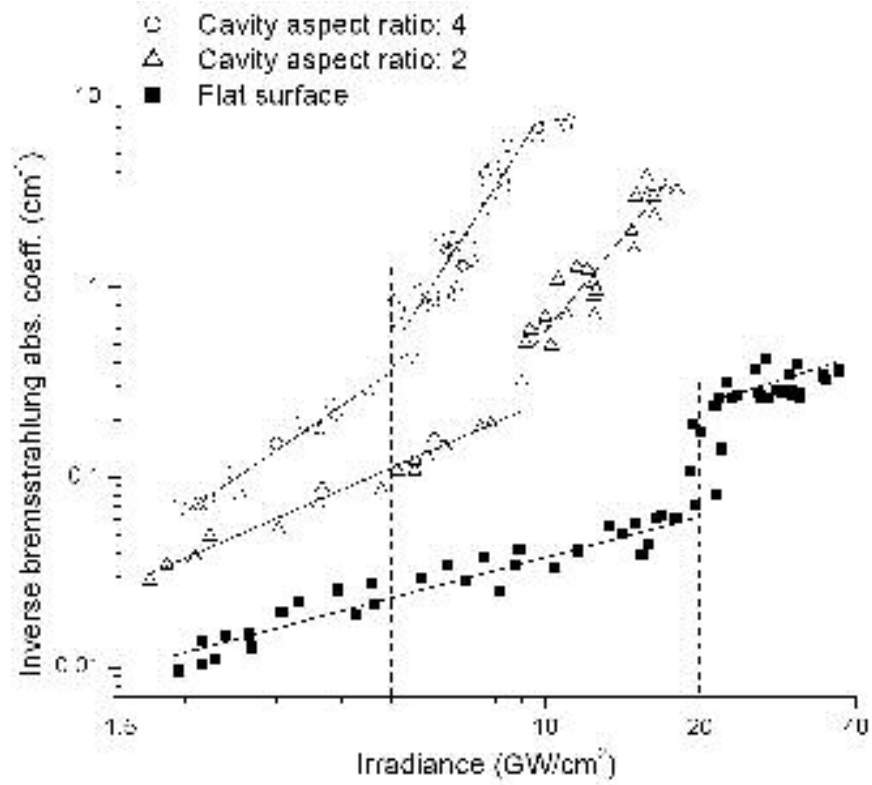


Figure 3.5 Inverse bremsstrahlung absorption coefficient at time of 30 ns and distance of 1 mm vs. irradiance.

Besides inverse bremsstrahlung, other mechanisms including photoionization, impact ionization and thermal ionization, may affect the absorption of the plasma [13]. The laser irradiance absorbed by the plasma can be expressed as [12]:

$$\Phi_{absorb} = \Phi(1 - \exp(-\alpha_p l)), \quad (3.15)$$

where l is the physical thickness and $\alpha_p l$ is the optical thickness of the plasma. The absorbed energy is converted into internal energy of the plasma. With increasing irradiance, the temperature and the degree of ionization of the vapor increase, which leads to additional plasma absorption.

Figure 3.6 shows crater depth changes with irradiance for laser ablation on the flat surface. The crater depth increased dramatically at the irradiance of ~ 20 GW/cm². As the irradiance was increased from 18 GW/cm² to 21 GW/cm², the crater depth abruptly increased from 1 to 10 μ m per pulse.

Figure 3.7 shows the images of ejected mass obtained by femtosecond laser shadowgraphy for laser irradiances below and above the threshold value, at time of 2 μ s after the laser pulse. At an irradiance slightly higher than threshold (Figure 3.7a), the image clearly shows the ejection of particulates in the size of several tens of microns. However, ejection of particulates was not detected for irradiances lower than threshold (Figure 3.7b). These data are consistent with the explosive boiling (phase explosion) study by J. H. Yoo, et al. [4].

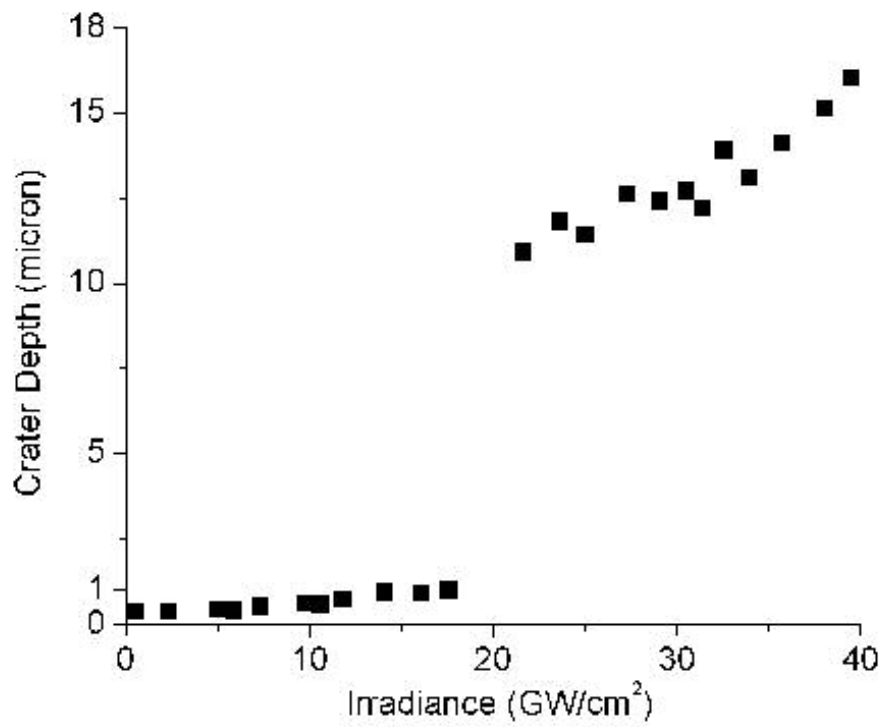
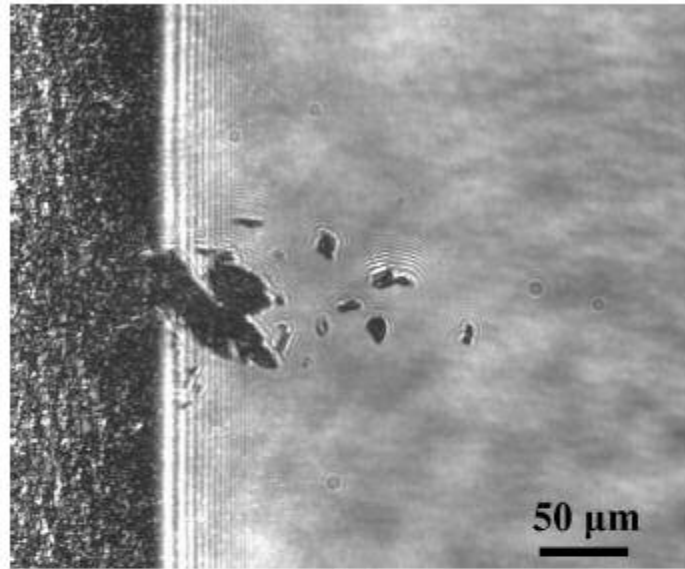
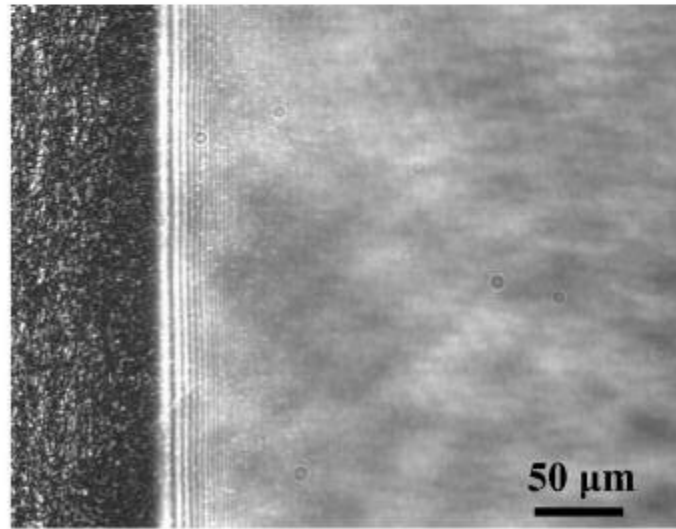


Figure 3.6 Crater depth resulting from single pulse laser ablation on fused silica vs. irradiance.



(a)



(b)

Figure 3.7 Images obtained by laser shadowgraphy for laser irradiances of (a) 21 GW/cm^2 and (b) 18 GW/cm^2 at time of 2 μs .

A possible mechanism for the large change of both plasma characteristics and mass removal when irradiance increases beyond a threshold is explosive boiling [14, 15]. Explosive boiling occurs when the sample is heated rapidly and the molten layer becomes superheated. Superheated liquid near the critical state experiences large density fluctuations. In the superheated liquid, these fluctuations can generate vapor bubbles. When vapor bubbles reach a critical radius, they expand spontaneously. The rapid expansion of these vapor bubbles in the superheated liquid leads to the ejection of particulates [4].

One possible explanation for the decrease of the threshold value in the cavity is self-focusing of the laser beam due to density gradient in the plasma. Hora [16] derived the laser power threshold for nonlinear-force self-focusing of a laser beam in a plasma:

$$P \geq \begin{cases} 1.46 \times 10^6 T^{-5/4} & \text{for } \omega_p \leq \omega \quad \text{and} \quad T \geq 10 \text{eV} \\ 1.15 \times 10^4 T & \text{for } \omega_p \ll \omega \end{cases}, \quad (3.16)$$

where P is laser power in watts, T is plasma temperature in eV, ω_p is the plasma frequency, $\omega_p = 8.9 \times 10^3 \cdot \sqrt{n_e}$ Hz, ω is the laser frequency.

The electron number density and plasma temperature obtained at 30 ns delay time at threshold irradiance ($\sim 5 \text{ GW/cm}^2$) are $\sim 2 \times 10^{19} \text{ cm}^{-3}$ and $\sim 3 \text{ eV}$ for the aspect ratio of 4 cavity. Using the relations $n_e \propto t^{-1.51}$ and $T \propto t^{-1.08}$ [4], the electron number density and plasma temperature at the time of termination of the laser pulse ($t = 3 \text{ ns}$) are estimated to be $\sim 6.5 \times 10^{20} \text{ cm}^{-3}$ and $\sim 36 \text{ eV}$. The

corresponding plasma frequency is $\sim 2.3 \times 10^{14} \text{ Hz}$. Since the 266nm laser frequency is $1.13 \times 10^{15} \text{ Hz}$, the first case in Eq. (3.16) is more suitable. For the threshold irradiance $\sim 5 \text{ GW/cm}^2$ with beam size $50 \mu\text{m}$, the corresponding laser power is $\sim 9.8 \times 10^4 \text{ W}$. The calculated $PT^{5/4}$ is $\sim 8.6 \times 10^6$, close to the criteria value in Eq. (3.16).

Due to radiation reflection and plasma confinement effects, plasma shielding causes increased temperatures and electron number densities for laser ablation in a cavity compared to a flat surface. The higher plasma temperature and electron number density in a cavity causes self-focusing of the laser by the plasma, producing higher laser light intensities. Thus phase explosion occurs at a lower laser energy. Therefore, the threshold value decreases for laser ablation in a cavity and the greater the cavity aspect ratio, the smaller the threshold.

3.4 Conclusions

The formation of a laser induced plasma inside a cavity was investigated and compared with laser ablation on a flat surface. Plasma temperature and electron number density both in the cavity and on the flat surface change dramatically after the laser beam reaches a threshold irradiance. The threshold irradiances are lower for laser ablation in the cavities than on the flat surface. The greater the cavity aspect ratio, the lower the threshold irradiance. After the irradiance reaches the threshold irradiance, ionization becomes saturated for both the cavity and flat surface. The crater depths were increased approximately by an order of magnitude

from the depths below the threshold value. Phase explosion was discussed to explain the large change of both plasma characteristics and mass removal when irradiance increases beyond a threshold value. Self-focusing of the laser beam could be responsible for the decrease of the threshold value in cavities.

REFERENCE

1. J.F. Ready, Effects of High-Power Laser Radiation (Academic, New York, 1971)
2. S. H. Jeong, R. Greif, R.E. Russo, J. Appl. Phys. **80**, 1996 (1996)
3. H.C. Liu, X.L. Mao, J.H. Yoo, R.E. Russo, Spectrochim. Acta Part B **54**, 1607 (1999)
4. J.H. Yoo, S.H. Jeong, R. Greif, R.E. Russo, J. Appl. Phys. **88**, 1638 (2000)
5. G.J. Bastiaans, R.A. Mangold, Spectrochim. Acta, Part B **40B**, 885 (1985)
6. H.R. Griem, Principles of Plasma Spectroscopy (Cambridge University Press, 1997)
7. Atomic Spectra Databases. Version 2.0. National Institute of Standards and Technology (NIST), USA, 1999. (<http://www.nist.gov>).
8. S. Tamaki, T. Kuroda, Spectrochimica Acta, **42B**, 1105 (1987)
9. A.A. Pupyshev, E.V. Semenova, Spectrochim. Acta Part B **56**, 2397 (2001)
10. H.R. Griem, Spectral Line Broadening by Plasmas (Academic, New York, 1974)
11. G. Befeki, Principles of laser plasmas (Wiley Interscience, New York, 1976)
12. R.K. Singh, J. Narayan, Phys.Rev. B **41**, 8843 (1990)
13. S.S. Harilal, C.V. Bindhu, Riju C. Issac, V.P.N. Nampoori, and C.P.G. Vallabhan, J.Appl.Phys. **82**, 2140 (1997)
14. A. Miotello and R. Kelly, Appl. Phys. Lett. **67**, 3535 (1995)
15. R. Kelly and A. Miotello, Appl. Surf. Sci. **96-98**, 205 (1996)

16. H. Hora, Plasma at High Temperature and Density: Applications and Implications of Laser-Plasma Interaction (Springer-Verlag, New York, 1991)

Chapter 4

Energy deposition and shock wave propagation during pulsed laser ablation in cavities

4.1 Introduction

Pulsed laser ablation of solids in an ambient gas generates a shock wave as a result of an explosive evaporation of the solid [1, 2]. Since energy coupling and plasma properties are related to the cavity aspect ratio, it is of interest to study how the shock wave propagation is influenced by the cavity aspect ratio.

Laser shadowgraph imaging is a useful technique to study plasma expansion during laser ablation. In laser shadowgraph imaging, a pump beam irradiates the sample while a probe beam passes the region above the focal point of the pump beam. The probe beam is then directed to the CCD camera to record the image of the laser-induced plasma. Mao [3] used this technique to study the early time air plasma during picosecond laser ablation.

In this chapter, the influence of crater formation on the shock wave propagation was studied. Shock wave propagation was measured utilizing the time-resolved shadowgraph imaging technique at different delay times. Laser-induced shock waves were compared from fused silica cavities with different aspect ratios to flat surface data. The energy driving the shock wave outside cavities was calculated based on blast wave theory and compared with flat surface results.

4.2 Experimental System

A schematic of the imaging experimental system is shown in Figure 4.1. A 266 nm laser with a 3-ns pulse width was used as the ablation laser. The laser beam was focused onto the sample with a quartz lens to a spot diameter of $\sim 40 \mu\text{m}$ in air at 1 atm pressure. A Spectra-Physics TSA high power femtosecond laser with a pulse duration of approximately 100 femtosecond (full width at half maximum) was used as the probe beam. The 800 nm beam of the femtosecond laser passes a potassium dihydrogen phosphate (KDP) crystal, forming a probe beam at 400 nm that is perpendicular to the ablation laser beam. The probe beam is directed to a charge coupled device (CCD) camera after passing through a narrowband 400 nm filter. By changing the delay time, the probe beam can be varied in time with respect to the ablation beam.

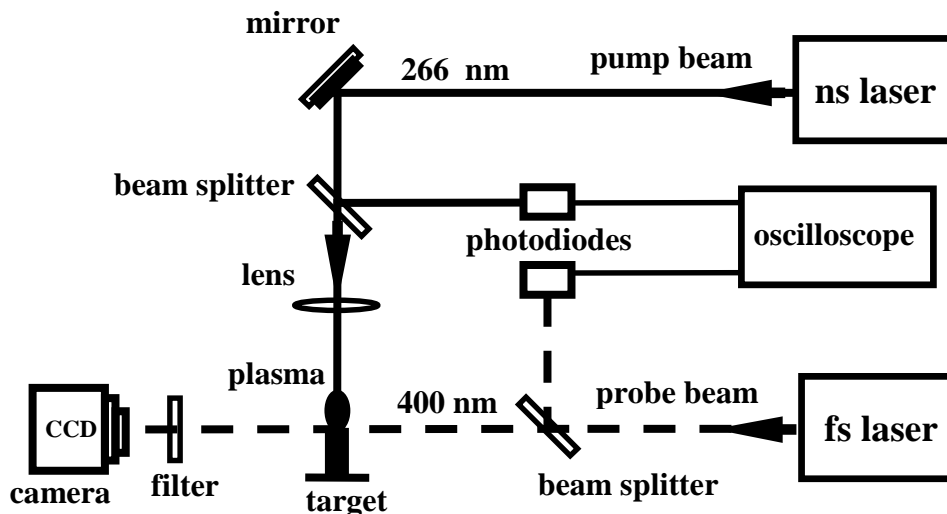


Figure 4.1. Schematic of the experimental setup for the pump-probe technique.

Fused silica glass was cut into samples of 5 mm width and 1 mm height, and placed on an *xyz* translation stage. Cavities were pre-fabricated using Gaussian-beam nanosecond laser ablation. Two cavities with the same diameter of about 80 μm , and different depths were obtained by repetitive laser ablation to produce aspect ratios of 3 and 6. Experiments were performed to record the shadowgraph images of the shock wave in the air and inside the fused silica. The spot size and energy (fluence) were equal when the laser beam was incident on the flat surface and on the bottom surface of each cavity.

4.3 Results and Discussion

4.3.1 Shadowgraph images of shock wave generated from laser ablation in cavities

Figure 4.2 shows time-resolved shadowgraph images of the shock waves in air and glass for laser ablation in a cavity and on a flat surface. The laser fluence was 40 J/cm^2 . The target surface is clearly shown as the black stripe, separating the glass on the left and the air on the right in the figure. Due to edge diffraction of the probe laser beam, there are weak fringes close to the target surface. After about 12 ns, the shock wave is seen outside the cavity with aspect ratio of 3 and becomes hemispherical after about 25 ns (Figure 4.2a). The shock wave generated on the flat surface expands spherically (Figure 4.2b).

The structure of the shock waves in air is similar to that reported by Salleo, et al. [4]. A thin layer of shocked air separates the shock front from the ionization

front. Between the ionization front and contact front is the shocked and ionized air. The contact front results from the expansion of ejected silica. Since the laser spot size is about 40 μm , the contact front is initially planar (Figure 4.2b).

For laser ablation on the flat surface (Figure 4.2b), the first acoustic wave is caused by thermalelastic expansion [5]. Due to the reflected internal shock inside the vapor plume [6], a second wave was generated inside the glass. As the high-pressure plasma expands inside the cavity, it generates acoustic wave inside the glass propagating cylindrically, compared with the hemispherical shock wave inside the glass generated by laser ablation at the bottom of the cavity. The speed of the wave propagating inside fused silica for both laser ablation inside cavities and on flat surface was calculated to be 5.85 $\mu\text{m}/\text{ns}$, close to the speed of sound in fused silica 5.76 $\mu\text{m}/\text{ns}$.

Figure 4.3 shows shadow graphs of shock waves generated inside a cavity with an aspect ratio of 6 at two different fluences. At a fluence of 40 J/cm^2 , it takes about 26 ns for the shock wave to expand out of the cavity. However, as the fluence is increased to 150 J/cm^2 , it only takes about 8 ns for the shock wave to expand out of the cavity. At higher fluences, the laser-generated plasma inside a cavity has much larger electron number density and to be at much higher temperature [7].

-
.

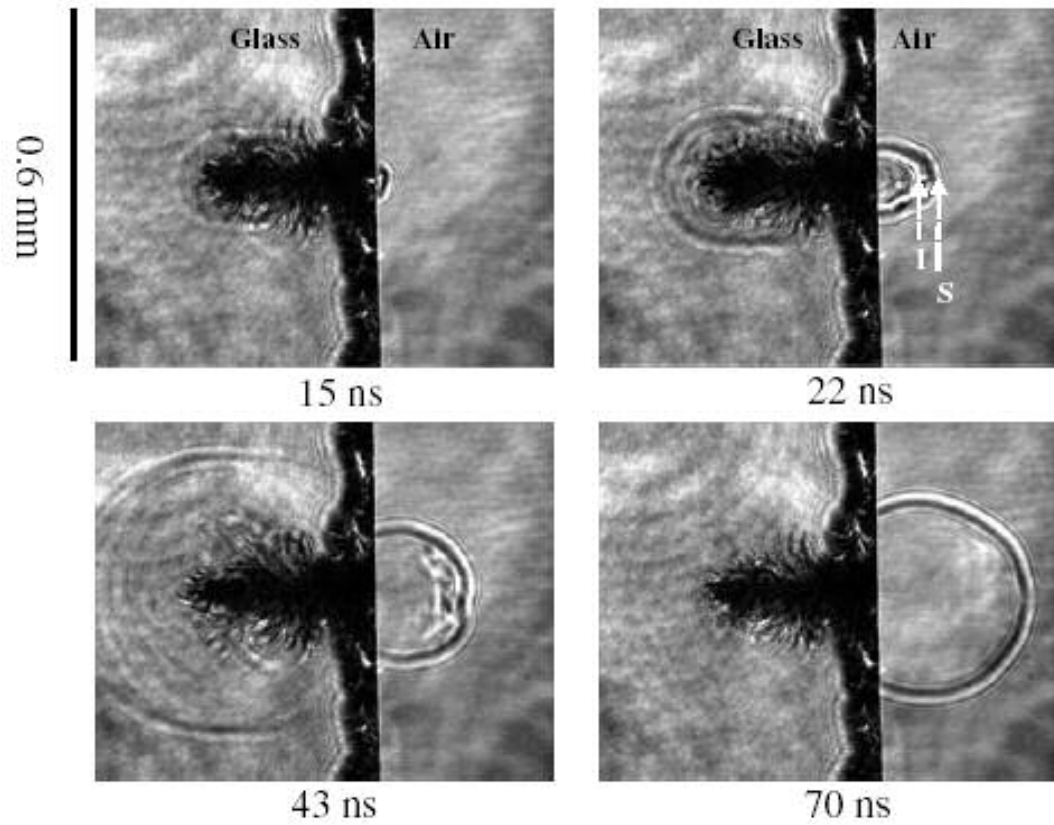


Figure 4.2 (a) Shadow-graphic images of shock wave generated from laser ablation in cavity. Cavity depth $240\ \mu\text{m}$, diameter $80\ \mu\text{m}$. The shock front (S) and the ionization front (I) are labeled in the figures.

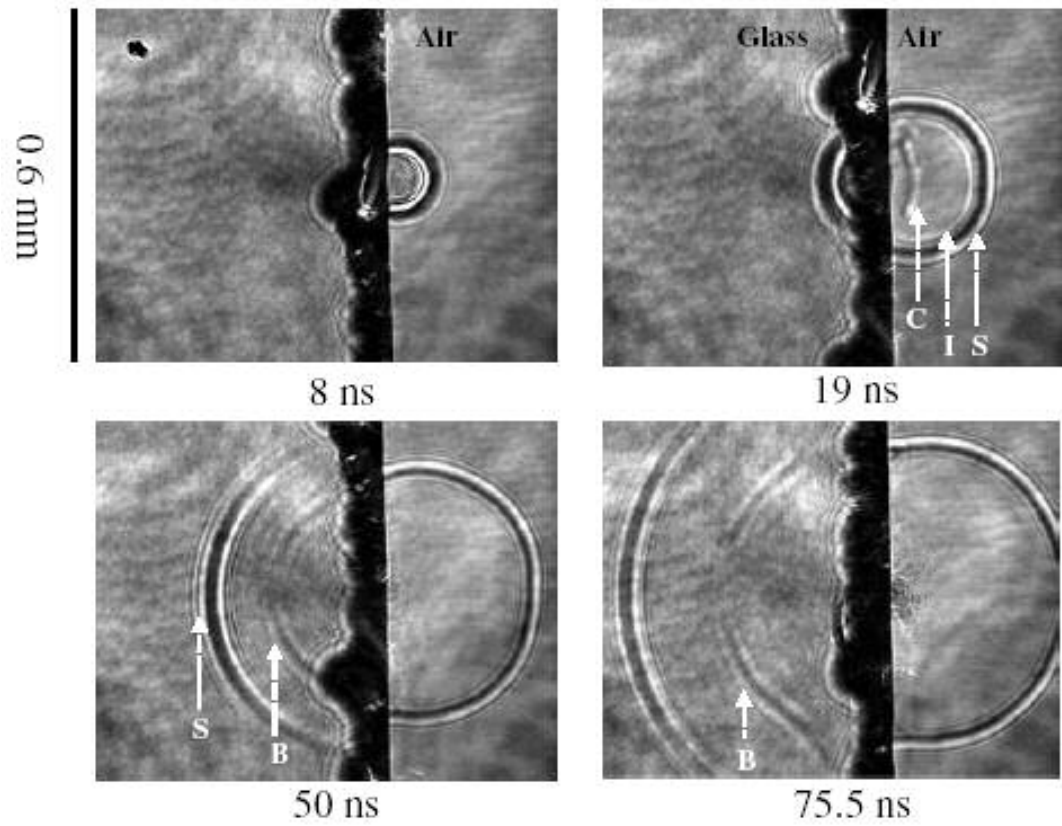


Figure 4.2 (b) Shadow-graphic images of shock wave generated from laser ablation on flat surface. The shock front (S), the ionization front (I), contact front (C) and back pressure induced shock wave (B) are labeled in the figures.

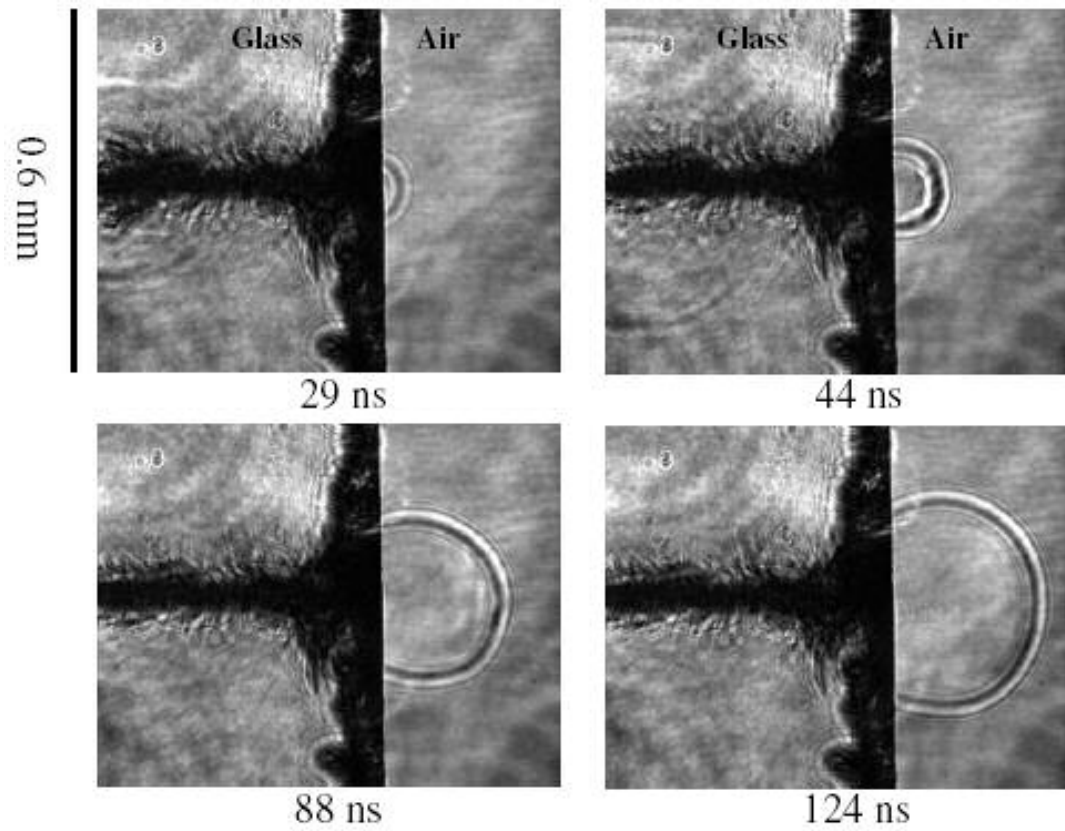


Figure 4.3 (a) Shadow-graphic images of shock wave generated from laser ablation in cavity at laser energy 0.5 mJ. Cavity depth 480 μm , diameter 80 μm . The detonation wave (D) and ejected materials (M) are labeled in the figures.

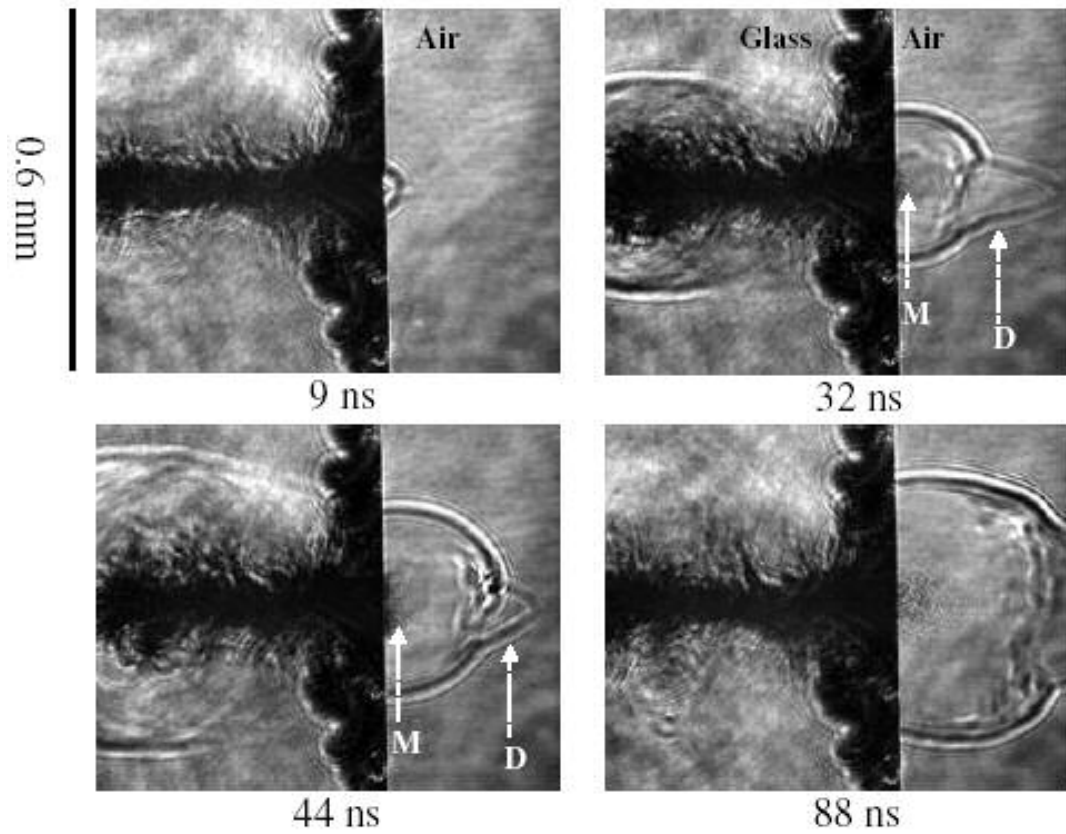


Figure 4.3 (b) Shadow-graphic images of shock wave generated from laser ablation in cavity at laser energy 1.9 mJ. Cavity depth 480 μm , diameter 80 μm . The detonation wave (D) and ejected materials (M) are labeled in the figures.

4.3.2 A modified blast wave equation for shock wave generated from laser ablation in cavities

The propagation of the laser-generated shock wave is approximated as resulting from an instantaneous, massless point explosion (blast wave) [8, 9]. The lateral distance R between the surface of the target and the position of a blast wave depends on the energy converted into the plasma state E . An analytical expression between R and E is given by the *Sedov–Taylor scaling* [10, 11]:

$$R = \lambda \left(\frac{E}{\rho} \right)^{1/(2+\beta)} t^{2/(2+\beta)} \quad (4.1)$$

where λ is a dimensionless quantity approximately equal to unity, ρ is the mass density of the undisturbed air and t is the time of propagation. The assumptions for the validity of this relation are that the pulse duration is shorter than t and the diameter of the spot area of the laser radiation is smaller than R . The parameter β represents the dimensionality of propagation (for spherical propagation $\beta = 3$, for cylindrical propagation $\beta = 2$ and for planar propagation $\beta = 1$).

Figure 4.4 shows that the radius R of the expanding shock wave from a flat surface is proportional to $t^{0.4}$, as predicted by Sedov's blast wave theory for spherical propagation. The energy that drives the shock wave propagation was calculated from Eq. 4.1 to be 0.24 mJ, or 48% of the incident laser energy.

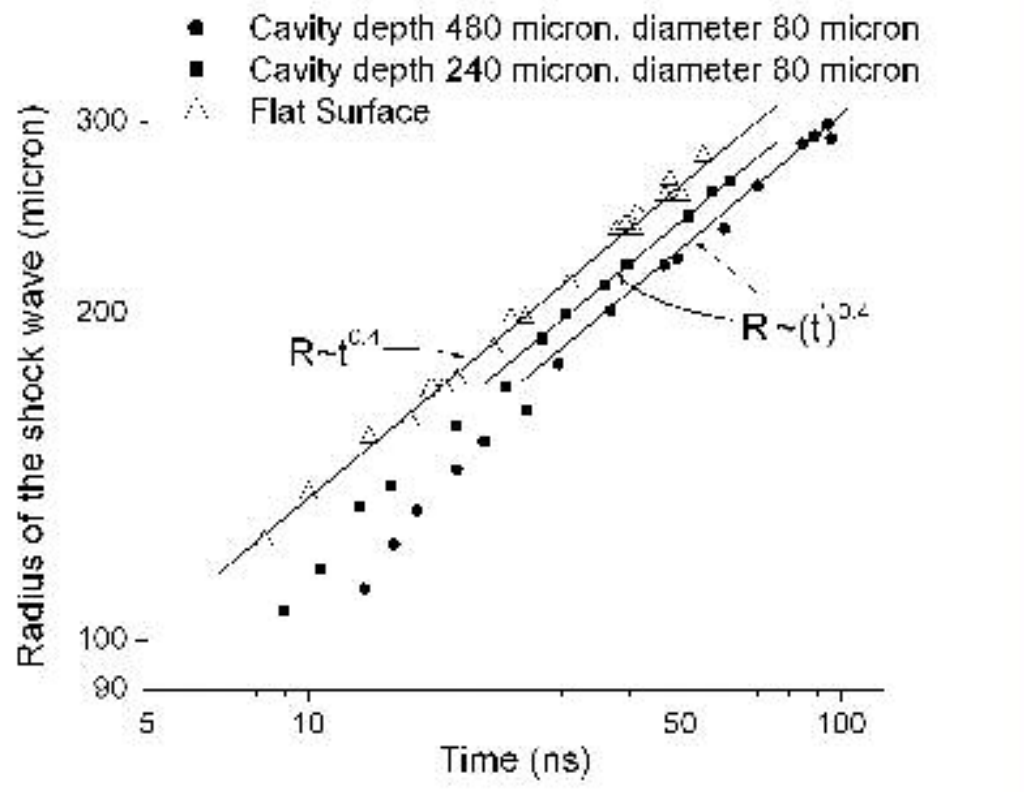


Figure 4.4 Air shock wave radius as a function of time for laser ablation in cavities and on flat surface (Equations 4.1 and 4.2).

For laser ablation in a cavity, a modified blast wave equation was proposed to describe the radius of the expanding shock wave:

$$R' = \lambda \left(\frac{E}{\rho} \right)^{1/(2+\beta)} (t')^{2/(2+\beta)}, \quad t' = t - t_0 \quad (4.2)$$

where R' is the lateral distance between the surface of the target and the position of the blast wave and t_0 is the time when the shock wave has just propagated outside of the cavity. For cavities with depths of 240 and 480 μm , t_0 approximately equals 12 and 26 ns, respectively. Inside the cavity, the shock wave propagation is confined by the cavity walls. After $t > t_0$, the shock wave propagation gradually changes to three-dimensional expansion. As shown in Figure 4.4, after $t' > 25$ ns for the cavity with aspect ratio of 3 and $t' > 35$ ns for the cavity with aspect ratio of 6, the radius of the expanding shock wave is proportional to $(t')^{0.4}$, corresponding to the spherical propagation of the blast wave ($\beta = 3$).

4.3.3 Thermodynamic properties of the shocked air

The pressure P_2 , density ρ_2 and temperature T_2 of the shocked air behind the shock front can be calculated by using the shock wave equations [10]:

$$\rho_2 = \frac{\gamma + 1}{\gamma - 1} \rho_1 \left[1 + \frac{2}{\gamma - 1} \frac{a_1^2}{c^2} \right]^{-1} \quad (4.3)$$

$$P_2 = \frac{2}{\gamma + 1} \rho_1 c^2 \left[1 - \frac{\gamma - 1}{2\gamma} \frac{a_1^2}{c^2} \right] \quad (4.4)$$

$$T_2 = \frac{P_2}{R\rho_2} \quad (4.5)$$

where specific heat ratio $\gamma = 1.4$, density $\rho_l = 1.2 \text{ kg/m}^3$ and the speed of sound $a = 333 \text{ m/s}$ for air. The shock wave front velocity c was obtained by differentiating equation (4.1). The results (Table 4.1) showed that the calculated temperatures of the shocked air outside of the cavities are much higher than on the flat surface at a time of 20 ns after the shock wave expands outside of the cavities. These data are consistent with the spectroscopic measurement of the plasma temperatures resulting from laser ablation inside cavities in chapter 2. Due to reflection and confinement effects by the cavity walls and plasma shielding (absorption and/or reflection of the laser beam by the plasma), temperatures and electron number densities are higher for laser ablation in a cavity than on a flat surface. The cavity acts as a trap in which light energy of the trailing edge of the laser pulse can be efficiently absorbed by the confined laser plasma.

Table 1. Thermodynamic properties of the shocked air just behind the shock wave front at time of 20 ns after the shock wave expands outside of the cavity

	Shock wave front velocity (m/s)	Density (kg/m^3)	Pressure (atm)	Temperature (K)
Surface	3030	6.79	92	4700
Cavity, aspect ratio 3	3770	6.93	141	7100
Cavity, aspect ratio 6	3950	6.95	155	7800

For cavities with an aspect ratio of 3 and 6, the energy that drives the expansion of the shock wave outside of the cavities was calculated from Eq. 4.2 to be approximately 0.14 and 0.1 mJ, or 28% and 20% of the incident energy,

respectively. The fraction of laser beam energy expended in driving air shock waves outside of the cavity was lower than on the flat surface. The greater the cavity aspect ratio, the smaller the energy driving the shock wave. Once the plasma is generated in the cavity, its lateral expansion is confined by the cavity wall. Since the plasma temperature is higher than the surrounding cavity wall temperature, energy is transferred from the plasma to the cavity wall by radiation and other methods. Thus, less energy is available to support the air shock wave outside of the cavity, and the pressure and temperature of the shocked air dropped quickly.

4.4 Conclusions

Time-resolved images of shock wave generated during pulsed laser ablation in cavities were obtained with the laser shadowgraph technique. After about 30 ns, the temporal expansion of the radius of the shock wave outside of a cavity followed the relation for a spherical blast wave as predicted by the Sedov-Taylor solution. Due to cavity confinement effects, the pressure and temperature of the shocked air outside of the cavities were higher than those on the flat surface. The energy used to drive the shock wave outside the cavity was smaller than that on a flat surface; the greater the cavity aspect ratio, the smaller the energy supporting the shock wave. Energy transfer from the plasma to the cavity wall was discussed to explain the decrease of the energy driving the shock wave outside of the cavity.

REFERENCE

1. M.V. Allmen, A. Blatter, Laser-beam Interactions with Materials – Physical Principles and Applications, 2nd ed (Springer-Verlag, Berlin, 1995)
2. S.H. Jeong, R. Greif and R.E. Russo, Applied Surface Science **127-129**, 1029 (1998)
3. S.S. Mao, X.L. Mao, R. Greif and R.E. Russo, Appl. Phys. Lett. **76**, 31 (2000)
4. A. Salleo, F.Y. Genin, M.D. Feit, A.M. Rubenchik, T. Sands, S.S. Mao and R.E. Russo, Applied Physics Letters **78**, 2840 (2001)
5. Todd W. Murray and James W. Wagner, Journal of Applied Physics **85**, 2031 (1999)
6. N. Arnold, J. Gruber, and J. Heitz, Applied Physics A **69**, S87 (1999)
7. Xianzhong Zeng, Xianglei Mao, Samuel S. Mao, Jong H. Yoo, Ralph Greif and Richard E. Russo, Journal of Applied Physics **95**, 816 (2004)
8. S.H. Jeong, R. Greif and R.E. Russo, J. Phys. D: Appl. Phys. **32**, 2578 (1999)
9. M. Aden, E.W. Kreutz, H. Schluter and K. Wissenbach, J. Phys. D: Appl. Phys. **30**, 980 (1997)
10. L.I. Sedov, Similarity and Dimensional Methods in Mechanics (Cleaver Hume, London, 1959)
11. Gert Callies, Peter Berger and Helmut Hugel, J. Phys. D: Appl. Phys. **28**, 794 (1995)

Chapter 5

Investigations of ablation efficiency and plasma expansion during ultraviolet femtosecond and nanosecond laser ablation of silicon

5.1 Introduction

In the previous three chapters, we provided the experimental studies of plasma formation and expansion during pulsed laser ablation in cavities. In this chapter, mass removal and plasma expansion during femtosecond laser ablation were investigated.

Lasers with femtosecond pulse duration are of particular interest for ablation as the pulse duration is less than the typical thermalization characteristic time of a few picoseconds. Due to a much smaller thermal diffusion depth, high-precision ablation and minimal damage can be obtained with femtosecond lasers [1,2]. Because of its very short pulse duration, the laser beam does not interact with the laser-induced plasma. A shorter plasma lifetime was reported for infrared femtosecond laser induced plasma than in the case of longer laser pulses [3,4]. Absorbed laser energy is fully deposited into the target and higher efficiency of material ablation can be obtained [5].

The interaction of a high-energy ultraviolet (UV) pulsed laser beam with solid materials has been studied extensively at nanosecond time scales [6-9]. However, there only are few reports about UV femtosecond laser ablation of solids.

With small absorption and thermal diffusion lengths, UV femtosecond laser pulses can minimize thermal effects and be applied to direct fabrication of microstructures [10].

In this chapter, UV femtosecond laser ablation of silicon in air was performed and compared with UV nanosecond laser ablation. Laser ablation efficiency was compared by measuring crater depth as a function of pulse number. The laser-induced plasma properties were determined from spectroscopic measurements. Images of plasma expansion were recorded with the laser shadowgraph imaging technique.

5.2 Experimental System

A diagram of the spectroscopic experimental system is shown in Figure 2.1. A quadrupled Nd:YAG laser (Coherent, Infinity) operating at 266 nm with a 3-ns pulse-width and a Ti: sapphire femtosecond laser (Spectra-Physics, TSA) with a 100-fs pulse-width were used as the ablation lasers. The femtosecond laser beam at its fundamental wavelength (800 nm) passed a Third Harmonic Generator (Spectra-Physics, TP-1A) to form the 266 nm beam that was focused on the silicon sample with a quartz lens to a spot diameter of $\sim 50 \mu\text{m}$. The ambient air was at 1 atm. pressure. The laser energy was 220 μJ per pulse or $\sim 11 \text{ J/cm}^2$ for both the femtosecond and nanosecond laser tests. Single pulse laser ablation was performed on silicon samples.

The imaging experimental system is shown in Figure 4.1. In the first experiment, the nanosecond laser was used as the pump (ablation) beam and the femtosecond laser was used as the probe beam. The time delay between the fs probe beam and ns ablation beam was controlled using a delay generator (Stanford Research, DG 535). The actual delay time was measured using photodiodes. To obtain shadowgraphs of the femtosecond laser-induced plasma, a beam splitter and an optical delay stage were used (Figure 5.1). One femtosecond laser beam (266 nm) was used as the pump beam, and the other one (400 nm) was used as the probe beam which passed through the optical delay stage before being directed to the CCD camera. By moving the delay stage, the optical path of the probe beam was varied, which changed the time delay between the pump and probe beams. The time resolution achieved with the optical delay stage can be as small as 100 fs.

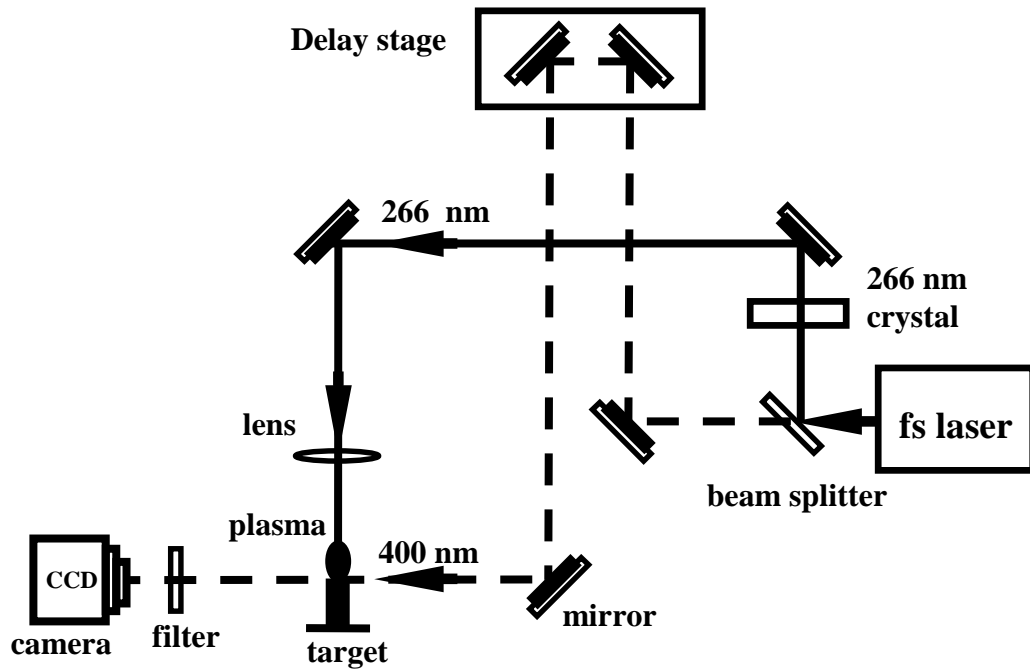


Figure 5.1. Schematic of the shadowgraph experimental setup for imaging of femtosecond laser-induced plasma.

5.3 Results and Discussion

5.3.1 Ablation depth

Figure 5.2 shows the dependence of crater depth on the laser pulse number. For both fs and ns laser ablation, the crater depth increases linearly with the pulse number for this low number of pulses. For the same number of laser pulses, however, the fs-crater is about two times deeper than the ns-crater using the same fluence. The nanosecond laser generated a significant raised rim caused by

resolidification of molten silicon. The rim around the fs-crater is much smaller than that of the ns-crater, indicating that melting was reduced using femtosecond pulses.

Scanning Electron Microscopy (SEM) images of the laser generated particles were shown in Figure 5.3. Particles from nanosecond laser ablation were mostly single large droplets ejected from the melted surface with diameters ranging from several hundreds nanometers to several microns. Primary particles generated using femtosecond laser ablation were small nano-sized spheres and agglomerates from these spheres, again suggesting that melting and ejection of molten mass is less for femtosecond laser ablation.

In the femtosecond regime, the laser pulse terminates before any material escapes from the surface. The laser energy is deposited in the sample target without a laser-plasma interaction. For nanosecond laser ablation, plasma shielding results in a decrease in the laser energy reaching the surface. Thus, the ablation efficiency decreases for nanosecond laser ablation [3].

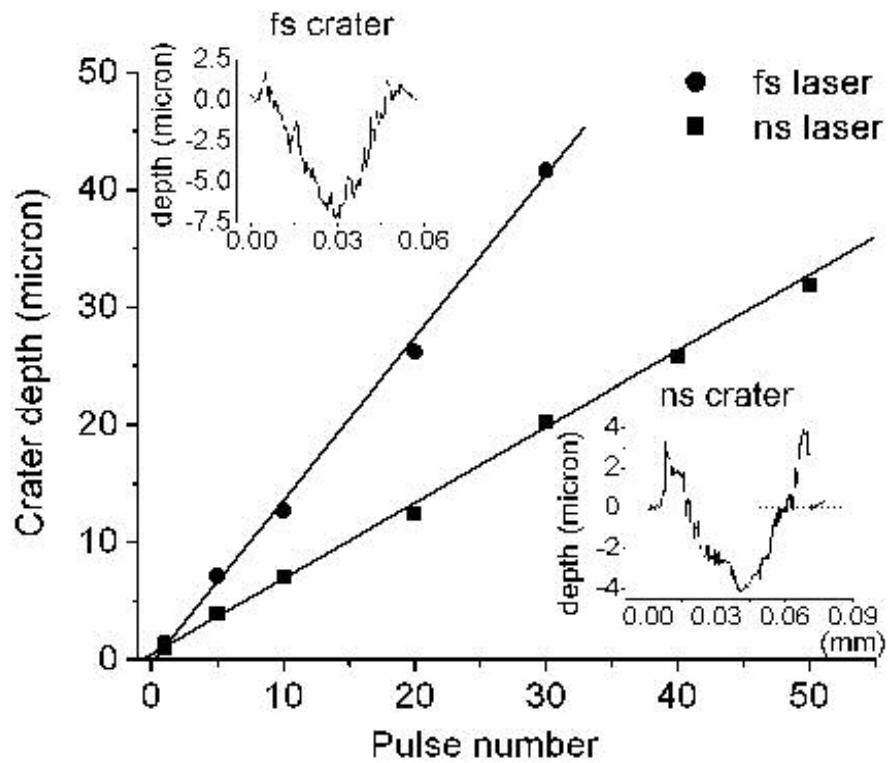


Figure 5.2 Ablation depth vs. pulse number for femtosecond and nanosecond laser ablation. The insets show the fs and ns crater profile after five laser pulses.

Figure 5.3 SEM images of laser generated particles for (A) nanosecond and (B) femtosecond laser ablation of silicon with 5000X magnification rate. Particles were collected on a silicon substrate.

Figure 5.3 SEM images of laser generated particles for (C) nanosecond and (D) femtosecond laser ablation of silicon with 20000X magnification rate.

5.3.2 Plasma temperature and electron number density comparison

As in chapter 2 and 3, the silicon emission line Si(I) at 288.16 nm was measured for diagnosing plasma properties (plasma temperature and electron number density). Figure 5.4 shows the time dependence of the Si line intensity measured with fs- and ns-pulses at a distance of 0.6 mm above the sample surface. After 30 ns, the emission intensities of both fs- and ns-plasma decrease exponentially. For small time (<30 ns), the emission intensity of the ns-plasma increases with time while the emission intensity of the fs-plasma decreases. At the beginning of the plasma expansion the ns-plasma becomes hotter because of absorption of the trailing part of the laser pulse via electron-neutral, electron-ion inverse bremsstrahlung and photoionization [11]. For the fs-pulse, the plasma expands without any other heating process and its emission intensity decreases.

Assuming local thermal equilibrium (LTE), the plasma temperature T can be determined by the relative line-to-continuum intensity ratio [12]. Stark line broadening from collisions of charged species is the primary mechanism influencing the emission spectra in these experiments [13,14]. A Lorentz function was used to fit the spectra and the Full Width Half Maximum (FWHM) of Stark broadened lines and the line to continuum emission ratio were obtained and were used to determine the electron number density and temperature of the plasmas [15].

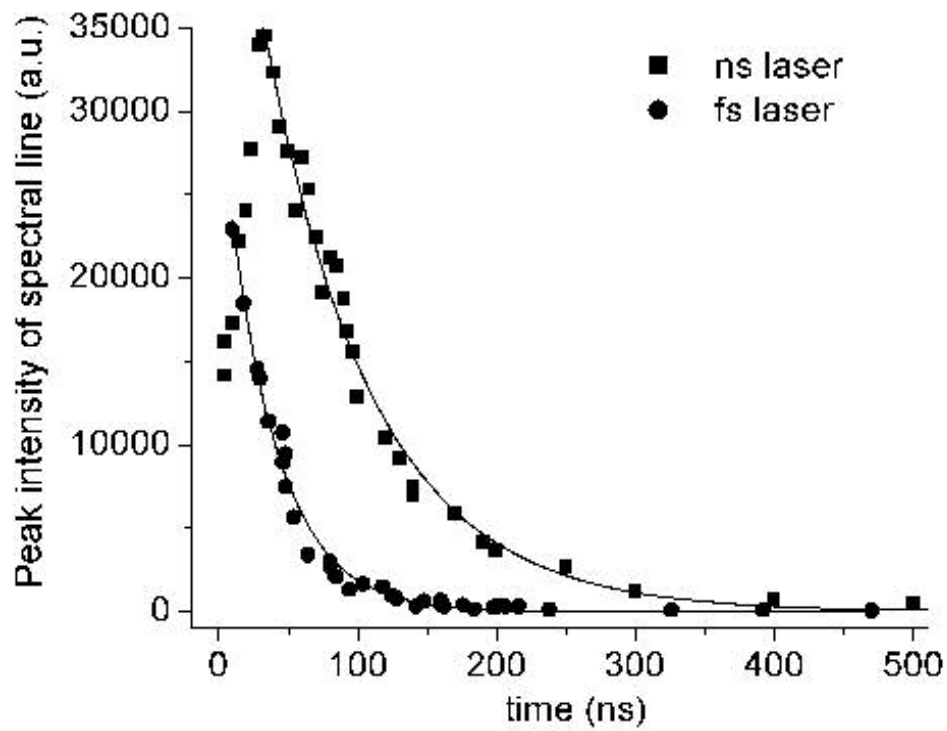


Figure 5.4 Peak intensity of Si (I) 288.16 nm emission line as a function of time for femtosecond and nanosecond laser ablation at a distance of 0.6 mm above the target surface.

The lower limit for the electron number density needed to collisionally maintain the energy-level populations to within 10% of LTE while competing with radiative decay is given by equation (2.8) (the McWhirter's criterion, [16]). At the highest temperature $kT = 3.4$ eV, the lower limit for n_e is $2.1 \times 10^{16} \text{ cm}^{-3}$, which is approximately two orders of magnitude lower than the value of n_e deduced from Stark broadening. Therefore, the validity of the LTE assumption is supported. However, it should be noted that the McWhirter's criterion is a necessary but not sufficient condition for LTE.

Figure 5.5 shows the temporal behavior of the electron number density and temperature of the fs-plasma and the ns-plasma. The density and temperature of the fs-plasma were less and decrease faster compared with ns-plasma due to different energy deposition mechanisms. At the femtosecond time scale, no laser-plasma interactions take place. Thus, the plasma cools quickly since no further energy is being supplied to the plasma. In contrast, a fraction of the laser energy is absorbed by the ns-plasma, which leads to greater plasma temperature and electron density. These results are consistent with ref. 6 which used femtosecond laser with 800 nm wavelength.

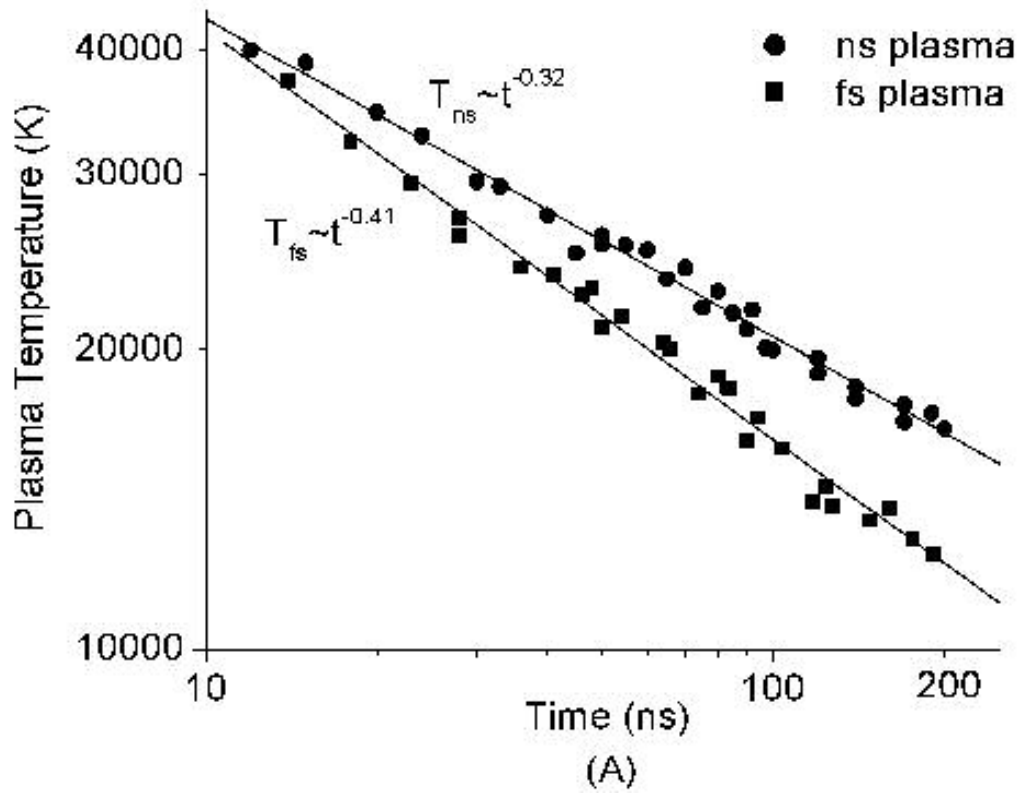


Figure 5.5 (A) Plasma temperature as a function of time for femtosecond and nanosecond laser ablation at a distance of 0.6 mm above the target surface.

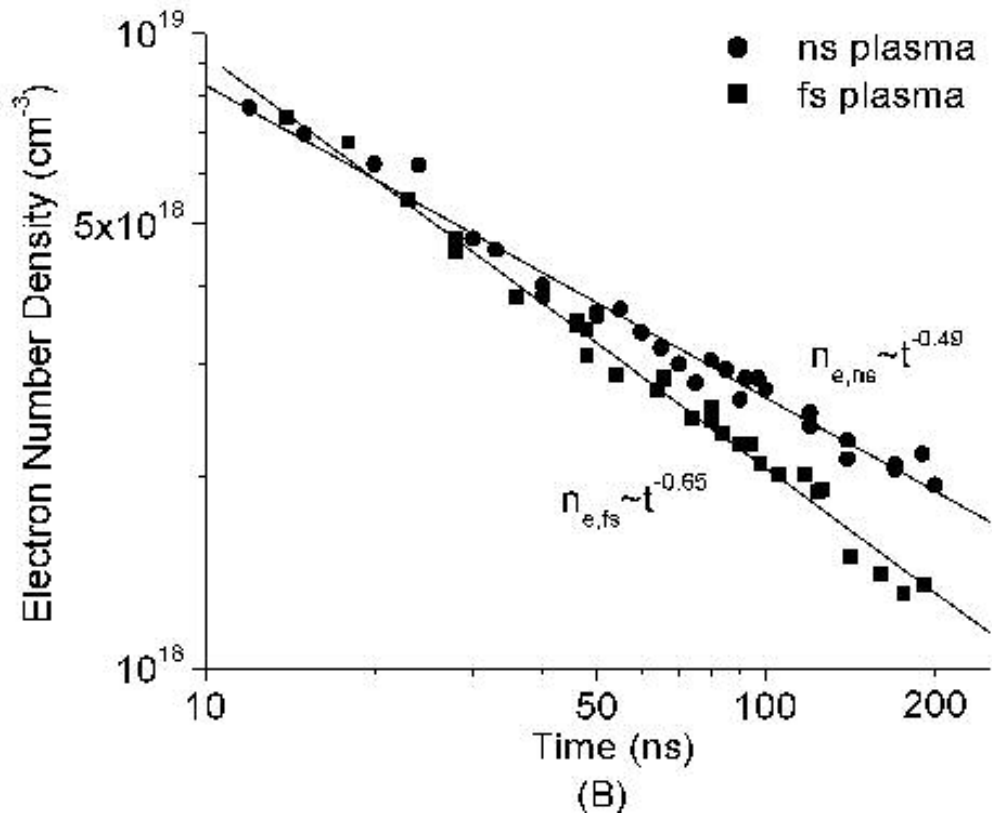


Figure 5.5 (B) Electron number density as a function of time for femtosecond and nanosecond laser ablation at a distance of 0.6 mm above the target surface.

5.3.3 Plasma expansion

Figure 5.6 shows shadowgraphs of the shock waves generated by femtosecond and nanosecond lasers 10 ns after the laser pulse. Due to edge diffraction of the probe laser beam, there are weak fringes close to the target surface. The structure of the shock waves in air is similar to that discussed in chapter 4. A thin layer of shocked air separates the shock front from the ionization front. Between the ionization front and contact front is the shocked and ionized air. Laser-induced air breakdown was seen for femtosecond laser ablation due to the much larger laser irradiance of 112 TW/cm^2 , compared with the irradiance of 3.7 GW/cm^2 for the ns laser.

Figure 5.7 shows shadowgraphs of the shock waves generated by femtosecond and nanosecond lasers at different times. The spatial and temporal scales of the images are different because of the different expansion properties for fs and ns laser-induced plasmas. The shock wave generated by the nanosecond laser expands spherically (Figure 5.7 e-h). Figure 5.8 (A) shows that the perpendicular expansion distance of the shock wave generated by the nanosecond laser is proportional to $t^{2/5}$, as predicted by Sedov's blast wave theory for spherical propagation; while the perpendicular location of the shock wave generated by the femtosecond laser is proportional to $t^{2/3}$, corresponding to one dimensional expansion. Lateral expansion distance of the shock wave as a function of time is shown in Figure 5.8 (B). At small times (less than 1 ns), the fs-plasma expanded primarily in the direction perpendicular to the target surface. After several

nanoseconds the fs-plasma expands in both the lateral and perpendicular directions. The expansion in the perpendicular direction was faster than in the lateral direction. For the ns laser, the laser-induced plasma expanded in both directions at similar velocities.

At 5 ns the perpendicular expansion velocities were $13.6 \times 10^5 \text{ cm/s}$ and $7.9 \times 10^5 \text{ cm/s}$ for fs- and ns-plasmas, respectively. The fs-plasma kinetic energy is therefore higher than the ns-plasma at small times. According to the shock wave equations [17], the pressure and temperature of the shocked air behind the shock front were calculated also to be higher for the fs case. As shown in Fig. 5, the plasma temperature of fs-plasma is approximately the same with the ns-plasma temperature at $\sim 15 \text{ ns}$. Since the temperature of the fs-plasma decreases faster than for the ns-plasma, the plasma temperature of fs-plasma would be higher at times earlier than $\sim 15 \text{ ns}$, which is consistent with the above velocity measurement.

5.4 Conclusions

Laser ablation efficiency and laser-induced plasma properties were studied for UV femtosecond and nanosecond laser ablation of silicon. Crater depth measurements showed that ablation efficiency was enhanced for UV femtosecond laser pulses. The electron number density and temperature were obtained from spectroscopic measurements and showed that the fs-plasma decreases faster than the ns-plasma. Laser shadowgraphy measurements of plasma expansion showed

that the femtosecond laser induced plasma expanded in one dimension at early times whereas the nanosecond laser induced plasma expanded in three dimensions.

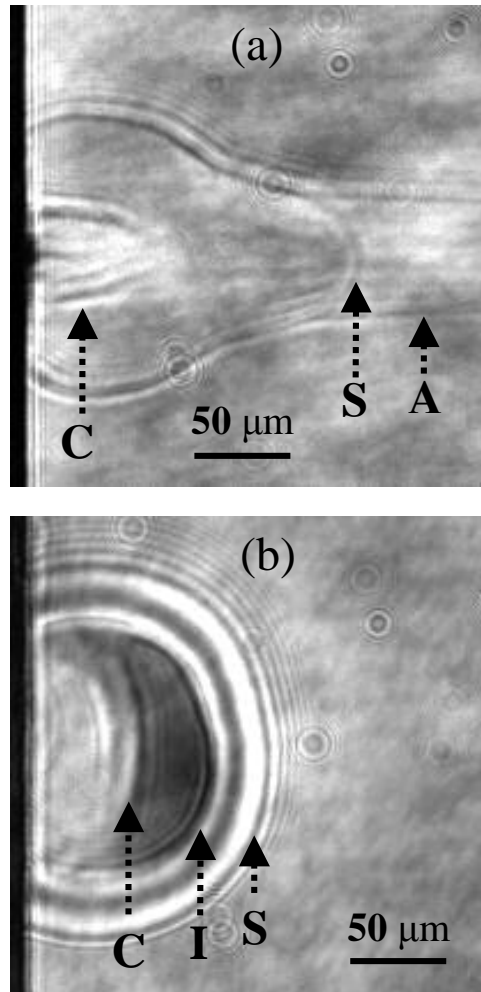


Fig. 5.6 Plasma images obtained by laser shadowgraphy for femtosecond (a) and nanosecond (b) laser ablation at 10 ns after laser shot. The shock front (S), ionization front (I), contact front (C) and air breakdown plasma (A) are labeled in the figures.

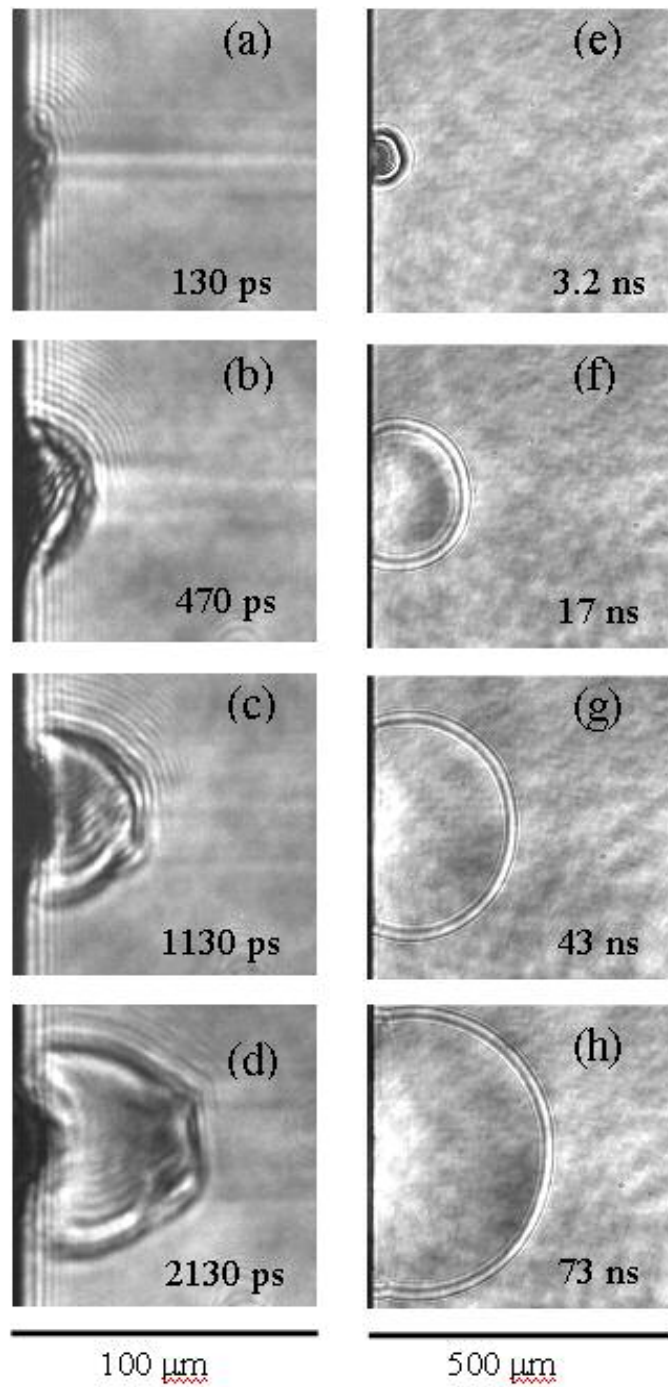


Figure 5.7 Sequence of shock wave images obtained by laser shadowgraphy for femtosecond (a-d) and nanosecond (e-h) laser ablation.

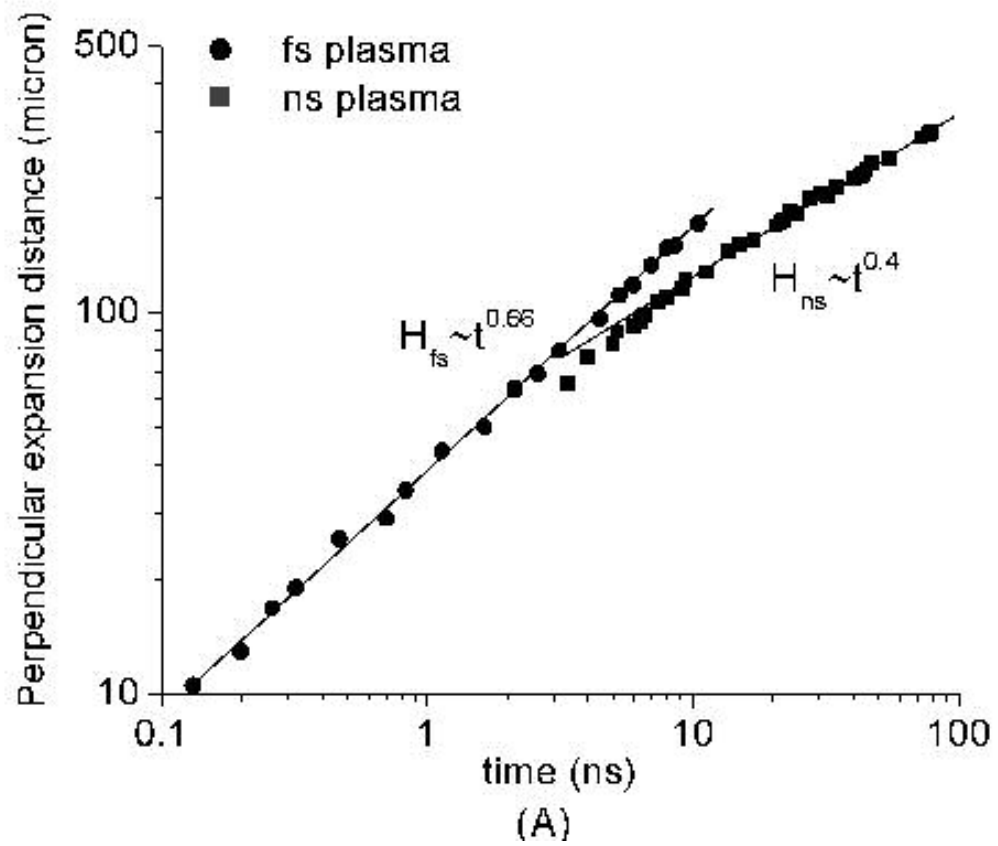


Figure 5.8 (A) Perpendicular expansion distance of shock wave as a function of time for femtosecond and nanosecond laser ablation.

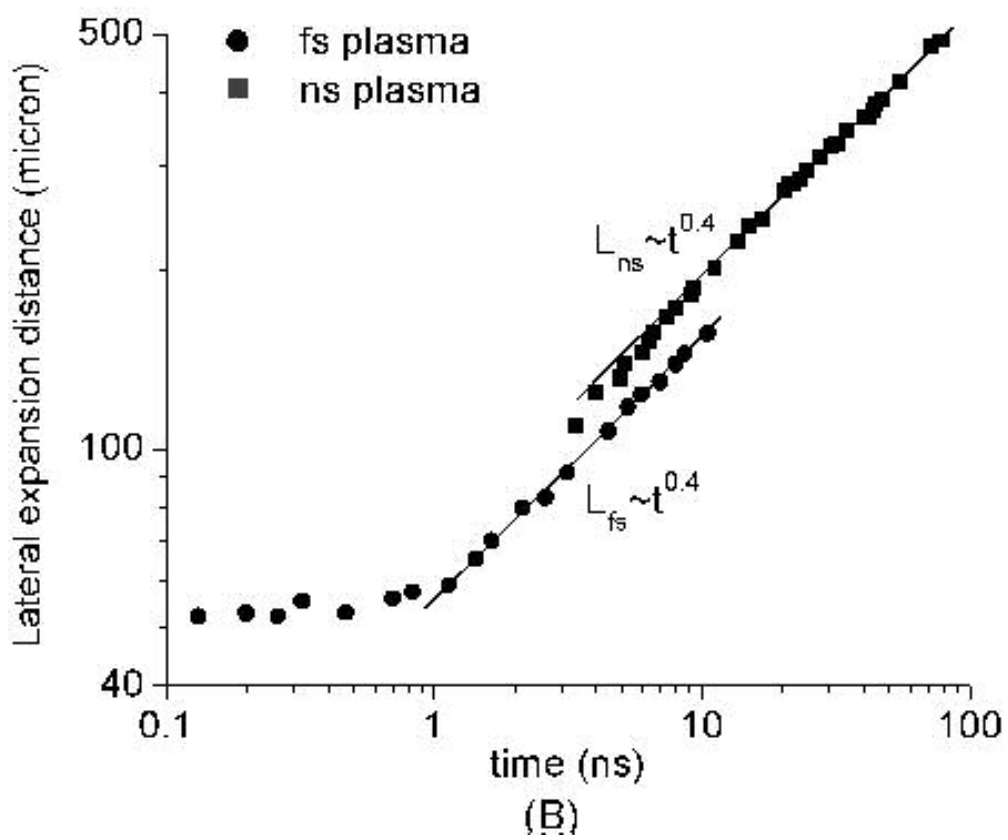


Figure 5.8 (B) Lateral expansion distance of shock wave as a function of time for femtosecond and nanosecond laser ablation.

REFERENCE

1. M. Lenzner, F. Krausz, J. Kruger and W. Kautek, Applied Surface Science **154-155**, 11 (2000)
2. P. Rudolph, J. Bonse, J. Kruger and W. Kautek, Applied Physics A **69**, S763 (1999)
3. B. Salle, O. Gobert, P. Meynadier, M. Perdrix, G. Petite and A. Semerok, Applied Physics A **69**, S381 (1999)
4. V. Margetic, A. Pakulev, A. Stockhaus, M. Bolshov, K. Niemax and R. Hergenroder, Spectrochim. Acta Part B **55**, 1771 (2000)
5. B. Le Drogoff, J. Margot, M. Chaker, M. Sabsabi, O. Barthelemy, T.W. Johnston, S. Laville, F. Vidal and Y. von Kaenel, Spectrochim. Acta Part B **56**, 987 (2001)
6. R.E. Russo, X.L. Mao, H.C. Liu, J.H. Yoo and S.S. Mao, Applied Physics A **69**, S887 (1999)
7. J.H. Yoo, S.H. Jeong, R. Greif and R.E. Russo, Journal of Applied Physics, **88** 1638 (2000)
8. S.H. Jeong, R. Greif and R.E. Russo, Applied Surface Science **129**, 177 (1998)
9. H.C. Liu, X.L. Mao, J.H. Yoo and R.E. Russo, Spectrochim. Acta Part B **54**, 1607 (1999)
10. I. Zergioti, S. Mailis, N.A. Vainos, A. Ikiades, C.P. Grigoropoulos and C. Fotakis, Applied Surface Science **138-139**, 82 (1999)

11. M.V. Allmen, *Laser-beam Interactions with Materials* (Springer-Verlag, New York, 1987)
12. G.J. Bastiaans and R.A. Mangold, *Spectrochim. Acta Part B* **40B**, 885 (1985)
13. G. Befeki, *Principles of laser plasmas* (Wiley Interscience, New York, 1976)
14. H.R. Griem, *Spectral Line Broadening by Plasmas* (Academic, New York, 1974)
15. Xianzhong Zeng, Xianglei Mao, Samuel S. Mao, Jong H. Yoo, Ralph Greif and Richard E. Russo, *Journal of Applied Physics* **95**, 816 (2004)
16. R.W.P. McWhirter, in: R.H. Huddlestone and S.L. Leonard (Eds.), *Plasma Diagnostic Techniques* (Academic, New York, 1965)
17. Xianzhong Zeng, Xianglei Mao, Sy-Bor Wen, Ralph Greif and Richard E. Russo, *Journal of Physics D: Applied Physics* **37**, 1132 (2004)

Chapter 6

Conclusions and Recommendations for Future Research

6.1 Conclusions

Cavity formation is a frequent result in many laser ablation applications. Although most theoretical investigations have been devoted to laser ablation on a flat surface, the development of a laser plasma inside a cavity is of both fundamental as well as practical significance.

In this study, we first determined the temperature and electron number density of laser-induced plasmas in fused silica cavities using spectroscopic methods. The effects of cavity aspect ratio on plasma properties were investigated. The temperature and electron number density of laser-induced plasma were measured to be much higher and to decrease faster for a plasma inside a cavity than on a flat surface. Reflection and confinement effects by the cavity walls and plasma shielding were discussed to explain increased temperature and electron number density with increasing cavity aspect ratio. The temporal variations of the plasma temperature and electron number density sharply decreased inside the cavity. An adiabatic expansion model was not suitable for the laser-induced plasma in the cavity because plasma wall interactions were not included.

We also investigated the effect of laser energy on the formation of a plasma inside a cavity. The temperature and electron number density of laser-induced plasmas in a fused silica cavity were compared with laser ablation on a flat surface. Plasma temperature and electron number density during laser ablation in a cavity

with aspect ratio of 4 increased faster with irradiance after the laser irradiance reached a threshold of 5 GW/cm^2 . The threshold irradiance of particulate ejection was lower for laser ablation in a cavity compared with that on a flat surface; the greater the cavity aspect ratio, the lower the threshold irradiance. The ionization of silicon becomes saturated and the crater depths were increased approximately by an order of magnitude after the irradiance reached the threshold. Phase explosion was discussed to explain the large change of both plasma characteristics and mass removal when irradiance increased beyond a threshold value. Self-focusing of the laser beam was discussed to be responsible for the decrease of the threshold in cavities.

Using the laser shadowgraph imaging technique, we studied the propagation of the shock wave generated during pulsed laser ablation in cavities and compared it with laser ablation on a flat surface. We found that outside the cavity, after about 30 ns the temporal expansion of the radius of the shock wave followed the relation for a spherical blast wave as predicted by the Sedov-Taylor solution. Due to cavity confinement effects, the pressure and temperature of the shocked air outside of the cavities were higher than those on the flat surface. The energy driving the shock wave outside the cavity was smaller than that on the flat surface; the greater the cavity aspect ratio, the smaller the energy supporting the shock wave. Energy transfer from the plasma to the cavity wall was discussed to explain the decrease of the energy driving the shock wave when it propagated outside of the cavity.

Lastly, laser ablation efficiency and laser-induced plasma properties were studied for UV femtosecond and nanosecond laser ablation of silicon. Crater depth measurements showed that ablation efficiency was enhanced for UV femtosecond laser pulses. The electron number density and temperature of fs-induced plasmas decreased faster than ns-induced plasmas due to different energy deposition mechanisms. Images of the laser-induced plasma were obtained with femtosecond time-resolved laser shadowgraph imaging. Plasma expansion in both the perpendicular and the lateral directions were compared for femtosecond and nanosecond laser ablation. At early times, the femtosecond laser induced plasma expanded in one dimension whereas the nanosecond laser induced plasma expanded in three dimensions.

6.2 Future Research

The present study showed that an adiabatic model was not suitable to describe a plasma in a cavity. To describe the processes for the development of a laser-induced plasma in a cavity including the sharp decrease of plasma temperature and electron number density, plasma wall interactions should be included in the analysis. Future studies should investigate the energy transfer from the plasma to the cavity wall. Further studies are needed to assess the electron heat conduction, electron-ion recombination and condensation of vapor on the cavity walls, and the plasma radiation effects on the laser ablation in the cavities. Numerical modeling of pulsed laser ablation in a cavity would be necessary. As an

initial study, a two-dimensional model including thermal and hydrodynamic effects in a cylindrical cavity is recommended.

Elemental depth profiling of solid samples is important for micro analytical applications. The information obtained from the spectroscopic investigation of laser ablation in cavity structures may provide a mechanism for the observed elemental fractionation phenomenon. Further studies of the correlation between laser ablation in cavities and elemental fractionation would be helpful to determine the cause of selective ablation of elements.

The experimental work presented in this dissertation should be useful for such applications as laser micro-fabrication. UV femtosecond laser pulses have the advantage of minimizing thermal effects and can be applied to direct fabrication of microstructures. It would be important to study UV femtosecond laser ablation in the cavity structures and identify material-specific laser and surrounding gas conditions to enhance the ablation efficiency.